

REPORT DOCUMENTATION PAGE

Form Approved
OMB No. 0704-0188

Public reporting burden of this collection of information is estimated to average 1 hour per response, including the time for reviewing instructions, searching existing data sources, gathering and maintaining the data needed, and completing and reviewing the collection of information. Send comments regarding this burden estimate or any other aspect of this collection of information, including suggestions for reducing this burden, to Washington Headquarters Services, Directorate for Information Operations and Reports, 1215 Jefferson Davis Highway, Suite 1204, Arlington, VA 22202-4302, and to the Office of Management and Budget, Paperwork Reduction Project (0704-0188), Washington, DC 20503.

1. AGENCY USE ONLY (Leave Blank)		2. REPORT DATE 12/22/95		3. REPORT TYPE AND DATES COVERED Final Technical 030192 to 123195	
4. TITLE AND SUBTITLE Deformation and Failure of Metal-Matrix Composites Under Dynamic Loads				5. FUNDING NUMBERS 61102F 2306 AS	
6. AUTHOR(S) R. W. Klopp, D. A. Shockey, J. E. Crocker, and J. H. Giovanola					
7. PERFORMING ORGANIZATION NAME(S) AND ADDRESS(ES) SRI International 333 Ravenswood Avenue Menlo Park, CA 94025-3493				AFOSR-TR-96 97 0022	
9. SPONSORING / MONITORING AGENCY NAME(S) AND ADDRESS(ES) Air Force Office of Scientific Research AFOSR/NE, Bldg. 410 Bolling Air Force Base Washington, DC 20332				10. SPONSORING / MONITORING AGENCY REPORT NUMBER F49620-92-C-0020	
11. SUPPLEMENTARY NOTES 19970117 086					
12a. DISTRIBUTION / AVAILABILITY STATEMENT Distribution Statement A. Approved for public release; distribution is unlimited.				12b. DISTRIBUTION CODE	
13. ABSTRACT (Maximum 200 words) SRI International conducted a three-year program of experiments, microstructural examinations, and analysis to determine the rate sensitivity of deformation and failure of metal-matrix composites (MMC) and to understand and model the role of interfaces and constituents on dynamic failure. Silicon-carbide fiber reinforced Timetal® 21S and Ti-15-3 matrices in three heat treatment conditions were studied. The work included dynamic fiber pushout experiments to measure dynamic interface strength, notched three-point-bend experiments with acoustic emission sensors to determine the static fracture resistance, and notched one-point-bend experiments to determine dynamic fracture resistance. Microstructural examinations were performed on transverse and longitudinal cross sections. The nature of interface failure, fiber failure, and matrix failure was established. A key finding was that toughening from fiber bridging is not obtained under bending loads. In bending, fibers fail well in advance of the crack tip and are thereby prevented from bridging matrix cracks. A two-dimensional finite element model of the composite was developed in which fibers, matrix, and interfaces in the vicinity of the notch root were modeled explicitly. The model can be used in parameter studies to investigate changes in interface and constituent properties, and loading rate, and hence assist in designing MMCs having tailored combinations of strength, toughness, and, particularly, greater resistance to bend failure.					
14. SUBJECT TERMS metal matrix composites, dynamic loading, fiber pushout, fracture mechanics, notched bend failure, finite element models, interface strength				15. NUMBER OF PAGES 78	
				16. PRICE CODE	
17. SECURITY CLASSIFICATION OF REPORT UNCLASSIFIED	18. SECURITY CLASSIFICATION OF THIS PAGE UNCLASSIFIED	19. SECURITY CLASSIFICATION OF ABSTRACT UNCLASSIFIED	20. LIMITATION OF ABSTRACT		

UNCLASSIFIED

SECURITY CLASSIFICATION OF THIS PAGE

CLASSIFIED BY :

DECLASSIFY ON :

SECURITY CLASSIFICATION OF THIS PAGE

UNCLASSIFIED

CONTENTS

Section	Page
REPORT DOCUMENTATION PAGE.....	i
LIST OF FIGURES.....	v
LIST OF TABLES	vi
ACKNOWLEDGMENTS	vii
1 INTRODUCTION	1
2 OBJECTIVES AND ACCOMPLISHMENTS.....	3
3 WORK PERFORMED AND RESULTS	5
Materials.....	5
Fiber Pushout Resistance.....	5
Fracture Resistance Measurements	24
Microfailure Characterization	31
Modeling	37
Summary of Results.....	42
4 DISCUSSION AND RECOMMENDATIONS FOR FURTHER STUDIES.....	45
5 PERSONNEL, ACTIVITIES, PUBLICATIONS, AND PRESENTATIONS.....	47
Personnel.....	47
Activities	47
Publications.....	47
Presentations.....	48
REFERENCES.....	49
APPENDIX: Maze [23] Input File for DYNA2D [21] Model of MMC Notched Bend Failure.....	A-1

FIGURES

Figure		Page
1	Ti-15-3 WD microstructure as-received.....	6
2	Ti-15-3 SM microstructure as-received	7
3	Ti-15-3 SB microstructure as-received.....	8
4	Sigma/Timetal® 21S microstructure as-received.....	9
5	Impact tester for dynamic fiber pushout experiments	11
6	Results of tube-on-tube impact to verify Hopkinson bar load cell.....	12
7	Results of dynamic pushout experiments on 508- μ m-thick specimens having SB microstructure.....	14
8	Results of dynamic pushout experiments on 533- μ m-thick specimens having SM microstructure	15
9	Results of dynamic pushout experiments on 330- μ m-thick specimens having WD microstructure.....	16
10	Results of dynamic pushout experiments on 368- μ m-thick specimens having WD microstructure.....	17
11	Results of dynamic pushout experiments on 533- μ m-thick specimens having WD microstructure.....	18
12	Results of dynamic pushout experiments on 762- μ m-thick specimens having WD microstructure.....	19
13	Results of dynamic pushout experiments on 1067- μ m-thick specimens having WD microstructure.....	20
14	Proximal and distal end of impacted fibers	21
15	Three-point- and one-point-bend specimens.....	25
16	Quasi-static three-point-bend test results for various microstructures.....	27
17	Dynamic one-point-bend test results for various microstructures.....	29
18	Cross section of the crack line region of WD microstructure, dynamically loaded.....	32

FIGURES

Figure		Page
19	Cross section of the crack line region, SM microstructure, statically loaded.....	33
20	Ti-15-3 SM microstructure failure phenomena.....	34
21	Cross section of the crack line region, σ_f /Timetal 21S microstructure, statically loaded.....	35
22	Finite element mesh.....	38
23	Deformed mesh at $t = 10 \mu s$	40
24	Deformed mesh at $t = 18 \mu s$	41
25	Comparison of strains from experiment and finite element model for SM microstructure.....	43

TABLES

Table		Page
1	Summary of pushout experiments.....	22
2	Results of toughness measurements.....	26
3	Material properties for the finite element model.....	39

ACKNOWLEDGMENTS

We thank Dr. T. Nicholas of the Air Force Wright Laboratory for periodic project reviews and assistance in procuring specimen materials. We thank Messrs. Tim Gabb and Brad Lerch of NASA Lewis Research Center for providing the Ti-15-3 composites and for helpful discussions and USAF Captain John Pernot, who generously provided the Timetal® 21S composite.

We thank Mr. John Moskito, Master of Science candidate in the Materials Science Department at San Jose State University, for his able metallography and careful observations. We gratefully acknowledge previous AFOSR sponsorship under which many of the techniques used in the current program were developed. We are also grateful to SRI personnel Tom Lovelace, Joe Regnere, Michael Merritt, John Stotts, and Dan Walter for machining and instrumentation.

Finally, we thank Ms. Bonnie Antoun of Rennsselaer Polytechnic Institute for the micrographs used in Figure 4, and for helpful discussions.

Section 1

INTRODUCTION

SRI International conducted a three-year program of experiments, microstructural examinations, and analysis to determine the rate sensitivity of deformation and failure of metal-matrix composites (MMCs) and to understand and model the role of interfaces and the interactive effects of constituents on the dynamic failure process in these materials. Because MMCs such as titanium reinforced with SiC fiber are lightweight and resistant to creep and oxidation, the Air Force is considering their use in gas turbines and for hypersonic aircraft skins. Titanium-matrix MMCs reinforced with silicon-carbide-fiber have been envisioned as replacements for nickel-based alloys in turbine engine applications. These applications require strength at startup and operating temperatures, fatigue resistance, and, as in aircraft skin applications, resistance to impact-induced damage leading to catastrophic failure. Impact loading such as that due to fragments occurs at isolated sites and results in localized bending. Thus, dynamic toughness under conditions of localized bending is needed.

Although the dynamic response of monolithic materials is reasonably well understood, the dynamic deformation and failure response of MMCs has remained largely unexplored. The multiconstituent features of heterogeneous materials such as MMCs may make them respond differently to high and low loading rates. At high loading rates, constituent and interface properties may change and interaction and failure micromechanisms may be different from those that govern at low loading rates. For example, thin films that have different chemistry and properties often exist at fiber/matrix interfaces. These films can localize the deformation and elevate the strain rate, and hence result in different failure responses under dynamic loads. Failure behavior at high loading rates is important, because turbine components and airframes may be hit by such things as sand particles, birds, turbine fragments, and weapon-launched projectiles. Our program produced an understanding of MMC failure in dynamic bend loading situations, and a finite element model for bend failure that can help develop strong and tough MMCs for the next generation of hypersonic aircraft.

Section 2

OBJECTIVES AND APPROACH

The objectives of this research were to determine the rate sensitivity of deformation and failure of MMCs, to understand the role of interfaces and the interactive effects of constituents on the dynamic failure process in these materials, and to develop a model to help materials scientists tailor MMCs for dynamic loading applications.

To accomplish these objectives, we undertook a program of fundamental experiments, microfailure examinations, and modeling of a Ti-15-3 titanium alloy (reinforced with SCS-6 silicon carbide fibers)¹ in three heat treatment conditions, and a Timetal® 21S titanium alloy (reinforced with Sigma silicon carbide fibers). All MMCs were unidirectional, continuous, fiber layups. The experiments included dynamic fiber pushout experiments to isolate the effects of loading rate on interface strength, static notched three-point bend experiments with acoustic emission (AE) sensors to determine the static fracture resistance and to determine the onset of internal damage, and dynamic notched one-point-bend experiments to determine the dynamic fracture resistance. We performed microstructural examinations using scanning electron microscopy (SEM) and optical microscopy of transverse and longitudinal cross sections. The nature and extent of interface failure, fiber failure, and matrix failure was established.

We developed a two-dimensional, finite element model of the composite in which fibers, matrix, and interfaces in the vicinity of the notch root were modeled explicitly. The model can be used in a parameter study to investigate the effects on strength and toughness of changes in interface and constituent properties, and of changes in loading rate. Hence, the model can help material designers improve the static and dynamic failure resistance of these MMCs. The model will aid in the search for design parameter combinations that optimize strength, toughness, and in particular, resistance to bend failure.

Section 3

WORK PERFORMED AND RESULTS

MATERIALS

We tested two metal-matrix composites. One was a Ti-15-3 (Ti-15V-3Al-3Cr-3Sn wt%) matrix reinforced with eight plies of continuous, unidirectional, SCS-6, silicon carbide fibers, and was about 1.7 mm thick. The other was a Timetal® 21S (β -21S) (Ti-15Mo-3Al-2.7Nb-0.2Si wt%) matrix reinforced with eight plies of continuous, unidirectional, Sigma fibers, and was about 2.1 mm thick. The SCS-6 fibers were 140 μ m in diameter and the Sigma fibers were 100 μ m in diameter. Both types of fiber, produced by chemical vapor deposition onto nonstructural cores, had carbon-rich coatings to reduce reaction with the matrix during consolidation and heat treatment.

The Ti-15-3 composite was obtained from NASA Lewis Research Center. The composite had three microstructures, designated WD, for weak ductile; SM, for strong medium ductile; and SB, for strong brittle.² The resulting matrix microstructures differed primarily in the nature and distribution of α precipitates within the β matrix. The WD had coarse α platelets, the SM had the same coarse platelets interspersed with finer platelets from a second aging step, and the SB had only fine α platelets. Figures 1-3 are micrographs of the WD, SM, and SB microstructures.

The Timetal® 21S composite was obtained from the Air Force Wright Laboratory. We tested only one microstructure, which was obtained from the as-pressed, solution-treated condition by heat treating in vacuum. Figure 4 shows micrographs of the Timetal® 21S composite. The primary purpose of the vacuum heat treatment was to drive off excess hydrogen, but it also served as an aging treatment, that was at the upper end of the range of recommended aging temperatures. The resulting microstructure was a mixture of coarse α grains in a matrix of β grains, as shown in Figure 4. The fibers of the Timetal® 21S composite were considerably less straight and were less uniformly distributed than those of the Ti-15-3 composite. Indeed, the surface of the as-received composite plate was corrugated, and the fibers in the interior roughly followed the corrugations.

FIBER PUSHOUT RESISTANCE

In fiber-reinforced composites, load is transferred between the fibers and matrix by shear forces acting on the sides of the fibers. When there is a crack in the matrix, these shear forces

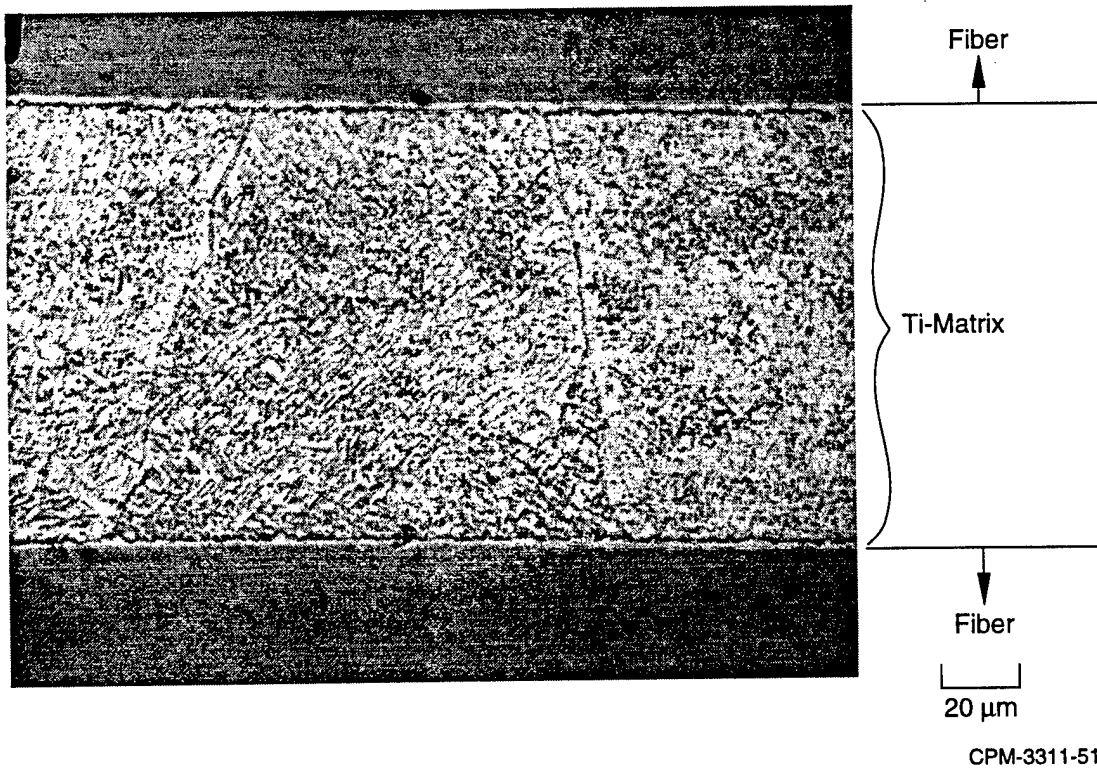
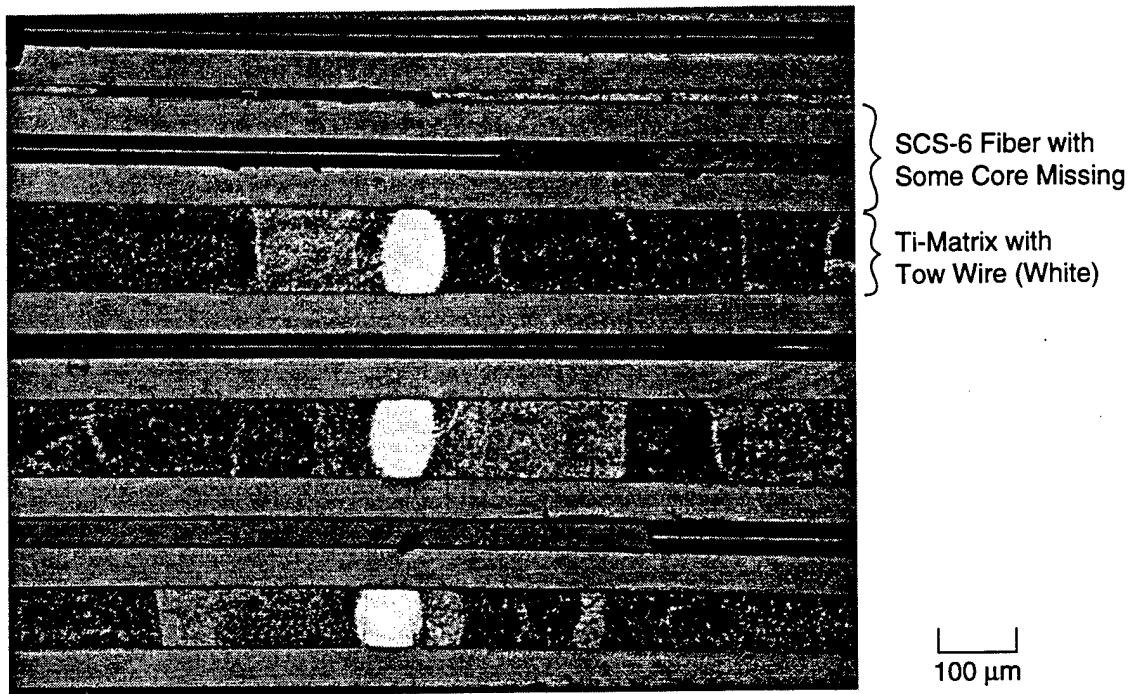


Figure 1. Ti-15-3 WD microstructure as-received.

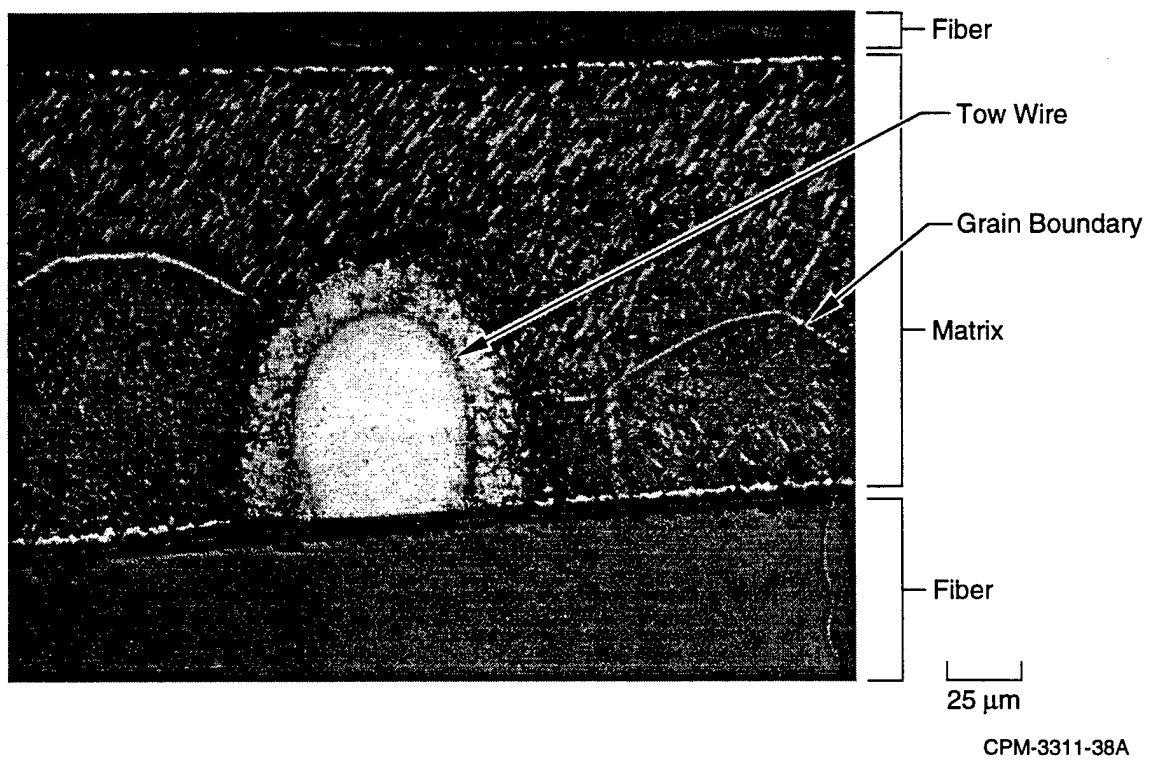
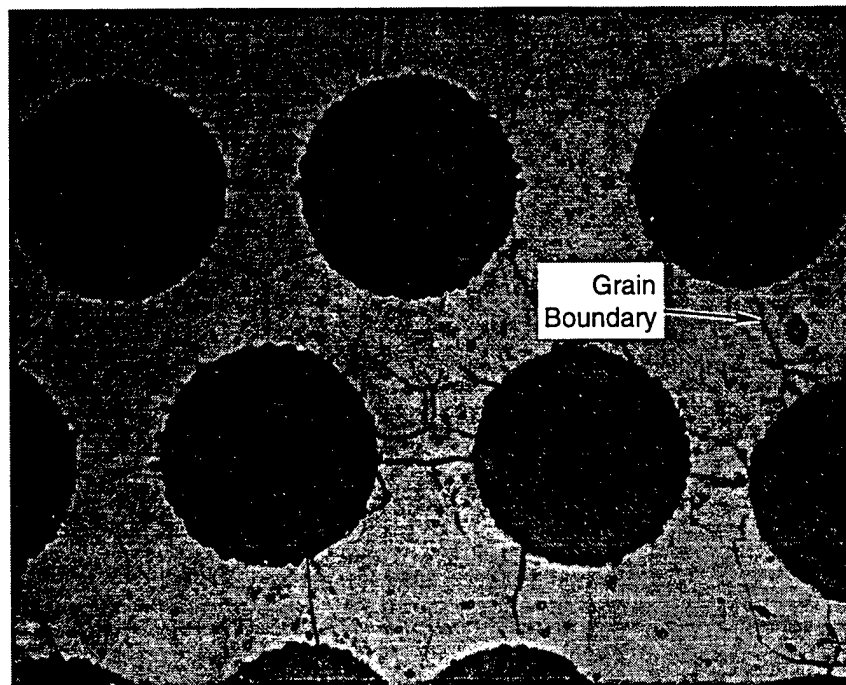
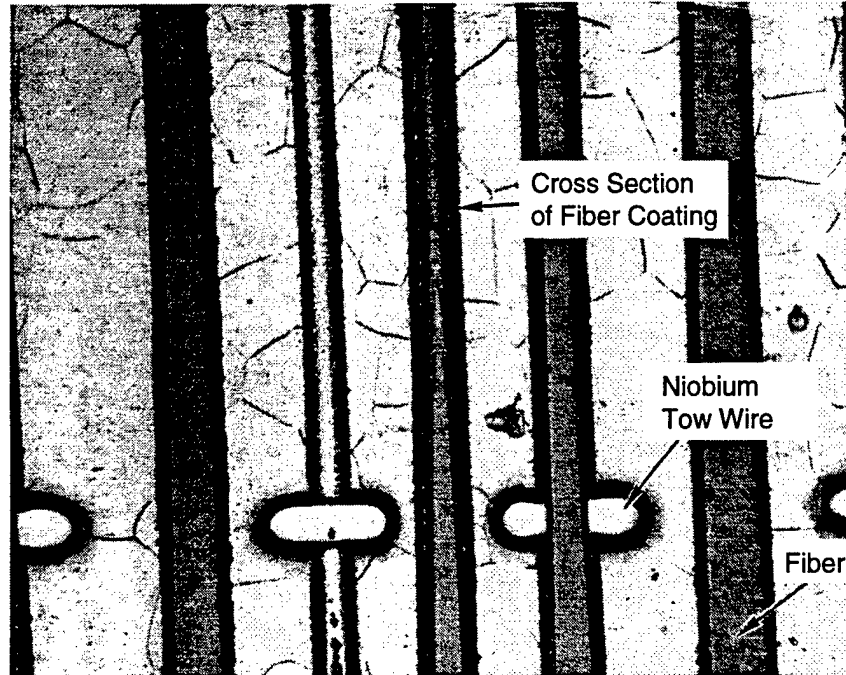


Figure 2. Ti-15-3 SM microstructure as-received.



CPM-3311-5A

Figure 3. Ti-15-SB microstructure as-received.

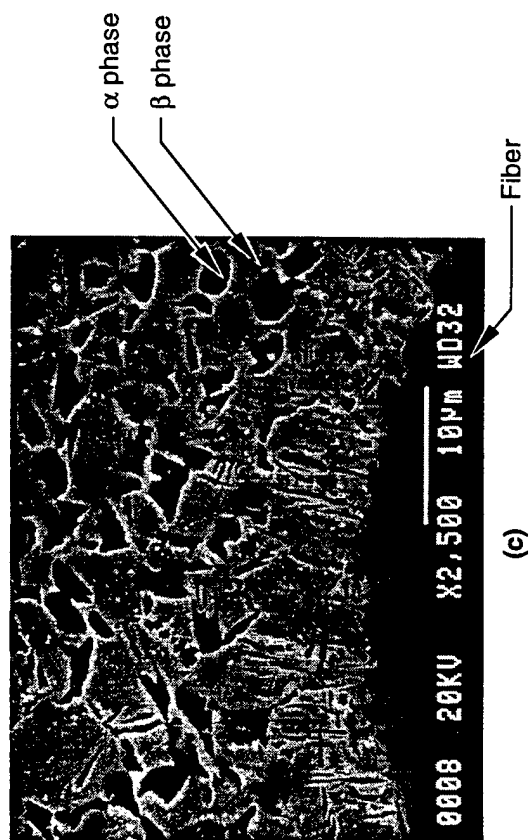
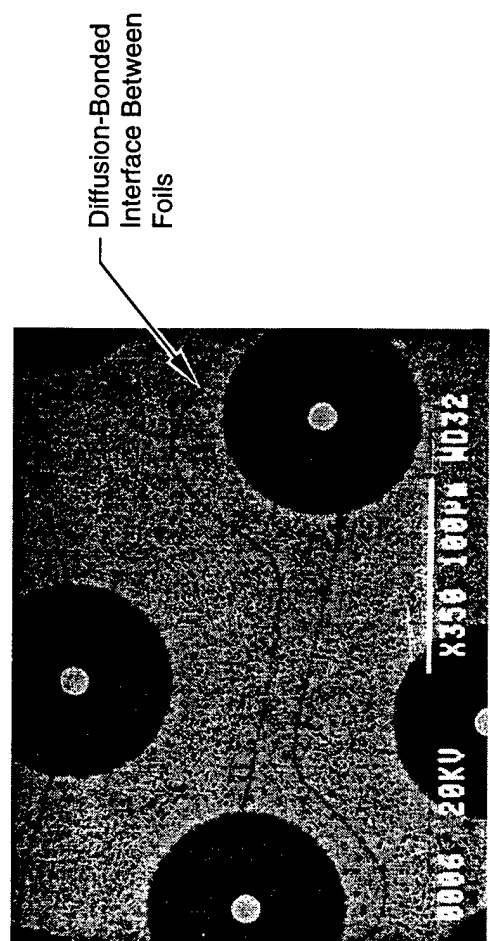
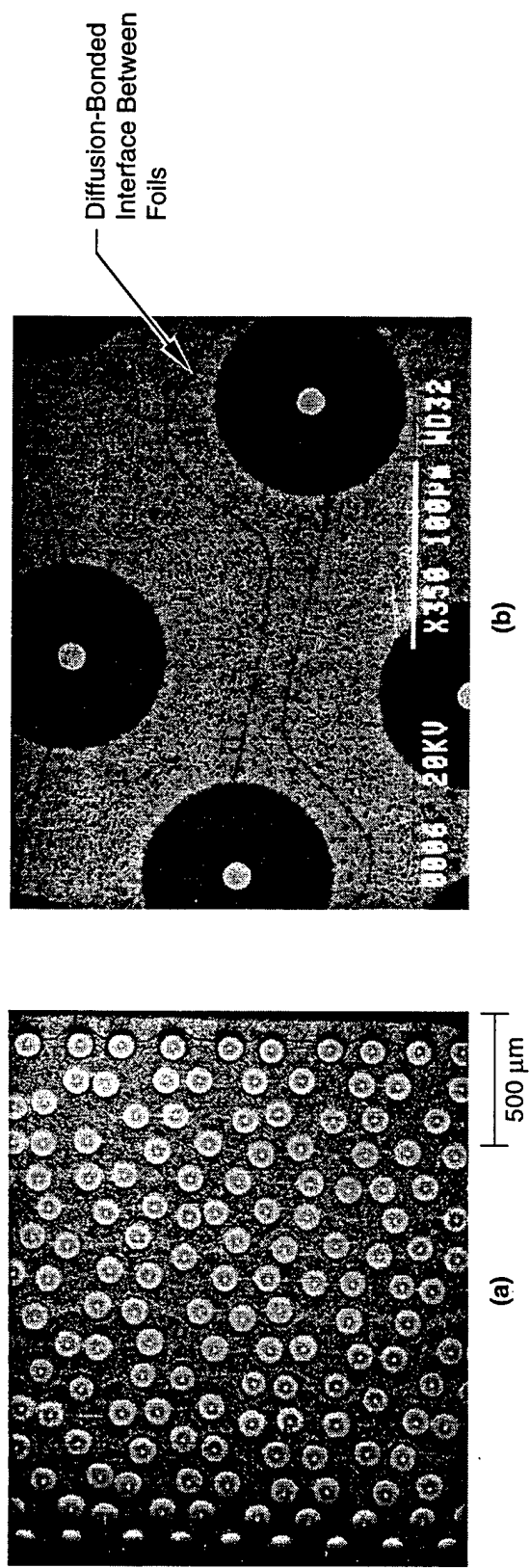


Figure 4. Sigma/TIMETAL ® 21S microstructure as-received.

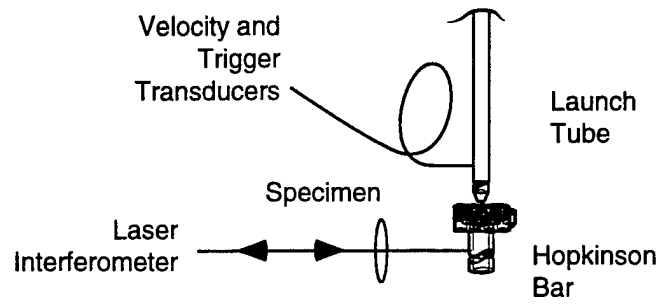
enable fibers that bridge the crack to limit crack opening. These forces also cause fiber tensile failure. Thus, the shear properties of the fiber/matrix interface, as well as the fiber tensile properties, are important to understanding cracking in composites, whether at quasistatic or dynamic loading rates.

Several analyses have established a connection between interface shear and composite fracture.³⁻⁶ Interface shear strength is directly related to the force required to push or pull a fiber out of the matrix. Force versus slip has been measured quasistatically using pushin,⁷ pushout,⁸ and pullout⁵ techniques. Analyses of these techniques that have appeared in the literature^{5,7-10} suggest that the pushout process has two phases: debonding and sliding. The analyses also suggest that characteristics of both phases can be obtained from measurements of the pushout force and fiber/matrix relative displacement. The analyses further suggest, however, that debonding occurs over very small relative displacements that may be difficult to resolve at high loading rates.

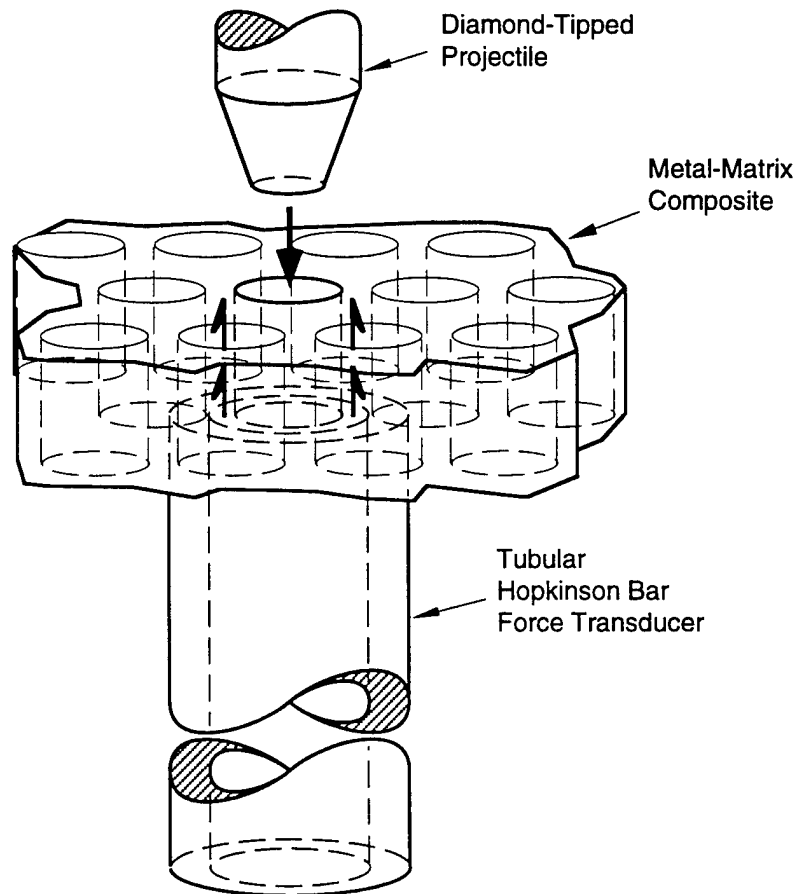
To our knowledge, no pushout measurements of MMCs have been made at loading rates higher than a few micrometers per second. Our objective was to measure the force versus sliding relation for the SCS-6/Ti-15-3 composites at high loading rates. Our approach was to develop an experiment wherein the end of a fiber is impacted with a projectile and the pushout force is deduced from the reaction force of the matrix against a tubular Hopkinson bar.

The experiment is shown schematically in Figure 5. In the experiment, a slice of composite a few hundred micrometers thick was cut with the fibers perpendicular to the cut faces. The slice was held horizontally by its edges and moved until it lightly contacted the end of a vertically oriented Hopkinson tube and a fiber was centered on the tube axis. The end of the fiber was impacted with a 2.6-g diamond-tipped projectile to push the fiber from the matrix into the tube. The projectile had a 100- μ m-diameter flat on its tip. The projectile velocity was obtained by timing the traversal of four machined grooves past a fiber optic probe. The projectile was launched by dropping it from various heights down a guide tube. The force was obtained by using a laser interferometer to measure the velocity pulse that propagates in the Hopkinson tube as it reacts against the matrix. Only about one in six impacts resulted in a successful measurement, either because the impact velocity was too low and the fiber failed to move, the projectile missed its target, or the data recorders failed to trigger at the appropriate time.

We verified the Hopkinson tube performance by performing an experiment for which a theoretical solution was available. We impacted a BeCu tube with a shorter piece of the same tubing without the lapped flats, and with no intervening slice of MMC. The waveform, Figure 6, showed that the pulse has a 6-8 μ s risetime prior to the achievement of theoretical load. Lee and



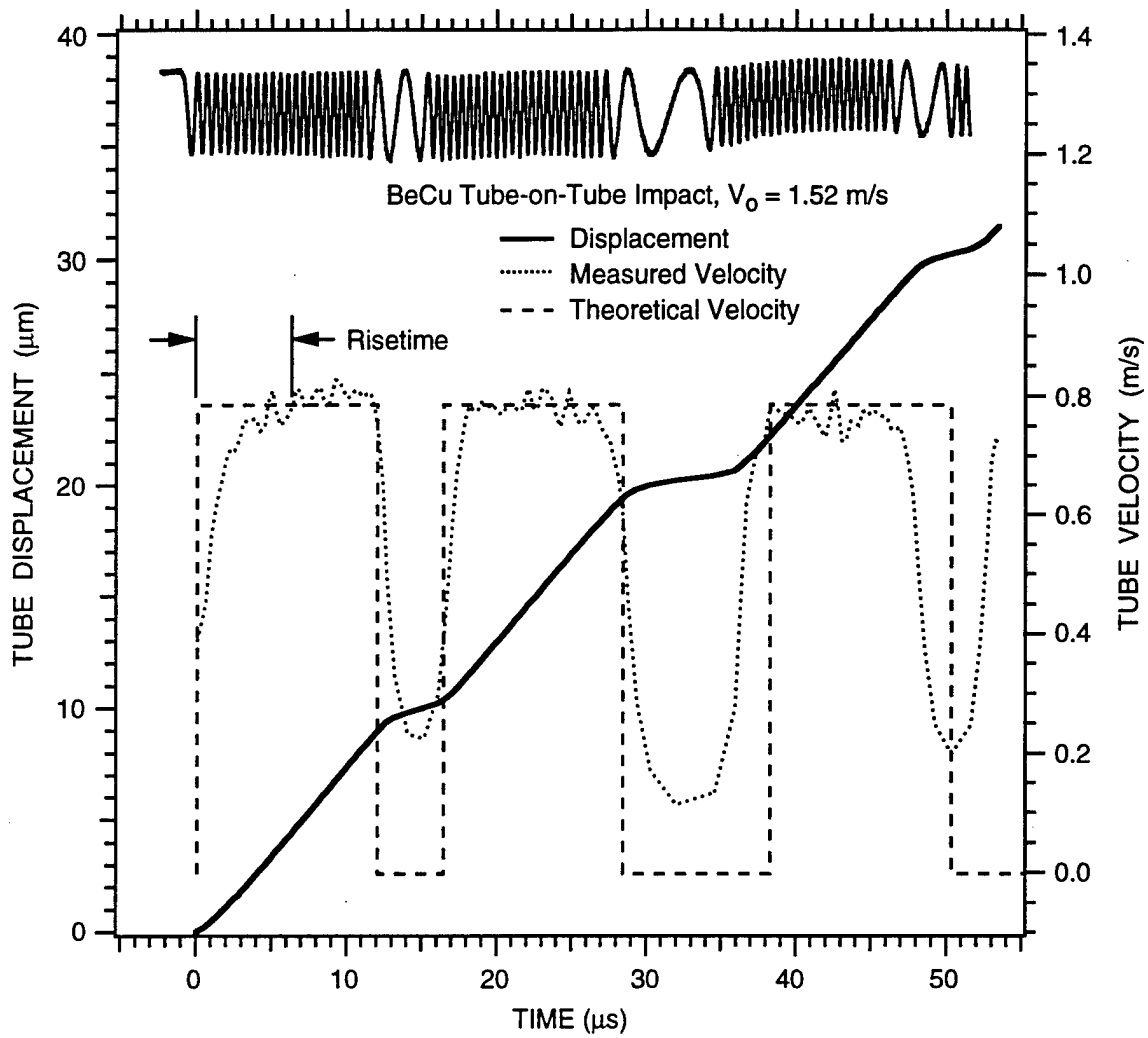
(a) Overall layout



(b) Projectile tip and Hopkinson bar force transducer

CAM-3311-11B

Figure 5. Impact tester for dynamic fiber pushout experiments.



CM-3311-53

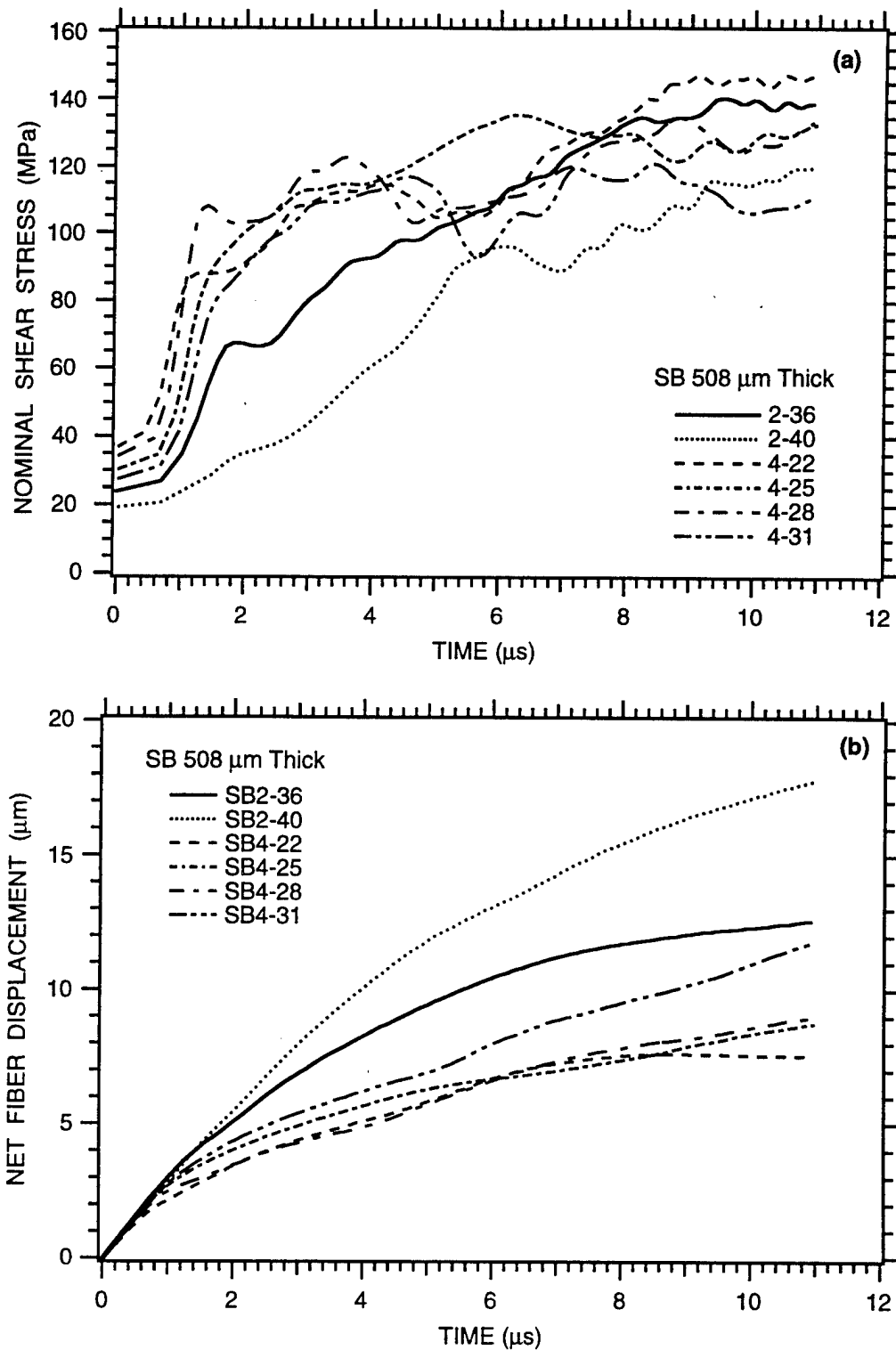
Figure 6. Results of tube-on-tube impact to verify Hopkinson bar load cell.

Crawford's Hopkinson bar dispersion analysis¹¹ suggests that a risetime of 200 ns is achievable in our experiment. The initial debonding event is not resolvable, but the tube-on-tube impact shows that a sliding force history can be measured accurately.

The MMC slices had large lateral dimensions relative to the fiber and Hopkinson tube radii. The portion of the slice beyond the tube radius was expected to support a part of the pushout load, with the balance supported by the tube. To quantify how much of the load "leaked" into the slice and was therefore unmeasured, we performed a finite element simulation of the experiment. The simulation showed that essentially all of the pushout load is reacted by the tube, because the tube is very stiff relative to bending of the MMC slice.

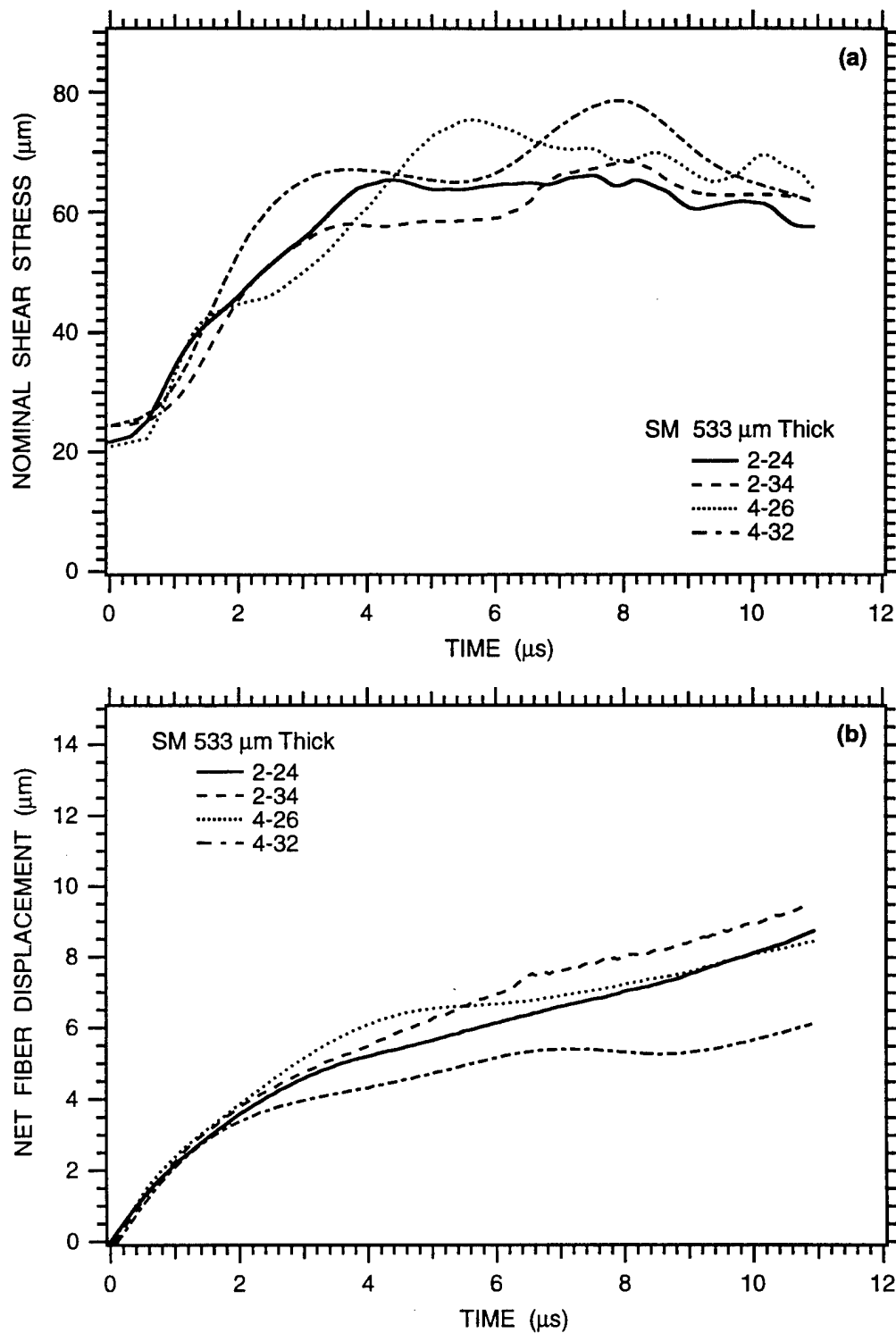
Figures 7-13 show the nominal shear stress and net fiber/matrix displacement histories for pushouts on slices of SB, SM, and WD microstructure. Because of dispersion, as shown by the risetime in Figure 6, rapidly-varying (high frequency content) features of the waveforms are lost and only the steady or relatively slowly varying portions of the waveforms beyond $\approx 8 \mu\text{s}$ provide a reliable measure of the pushout force. The net fiber displacement was obtained by subtracting the Hopkinson tube displacement from the projectile displacement, with the assumption that the relatively massive projectile maintains constant velocity, and the nominal shear stress was obtained by dividing the force by the net area of fiber in contact with the matrix (that is, the product of the fiber circumference and the slice thickness) and neglecting the movement of the fiber.

Table 1 summarizes the pushout experiments. In Table 1, the plus/minus variations in impact velocity, shear stress, displacement, and rate are simply the extremes of the data about the mean. We obtained the mean values by averaging the values at $10 \mu\text{s}$. By $10 \mu\text{s}$, the gross effects of dispersion have passed and the waveforms are steady or varying slowly and represent the true specimen response. Figure 14 shows the impacted and distal ends of typical fibers.



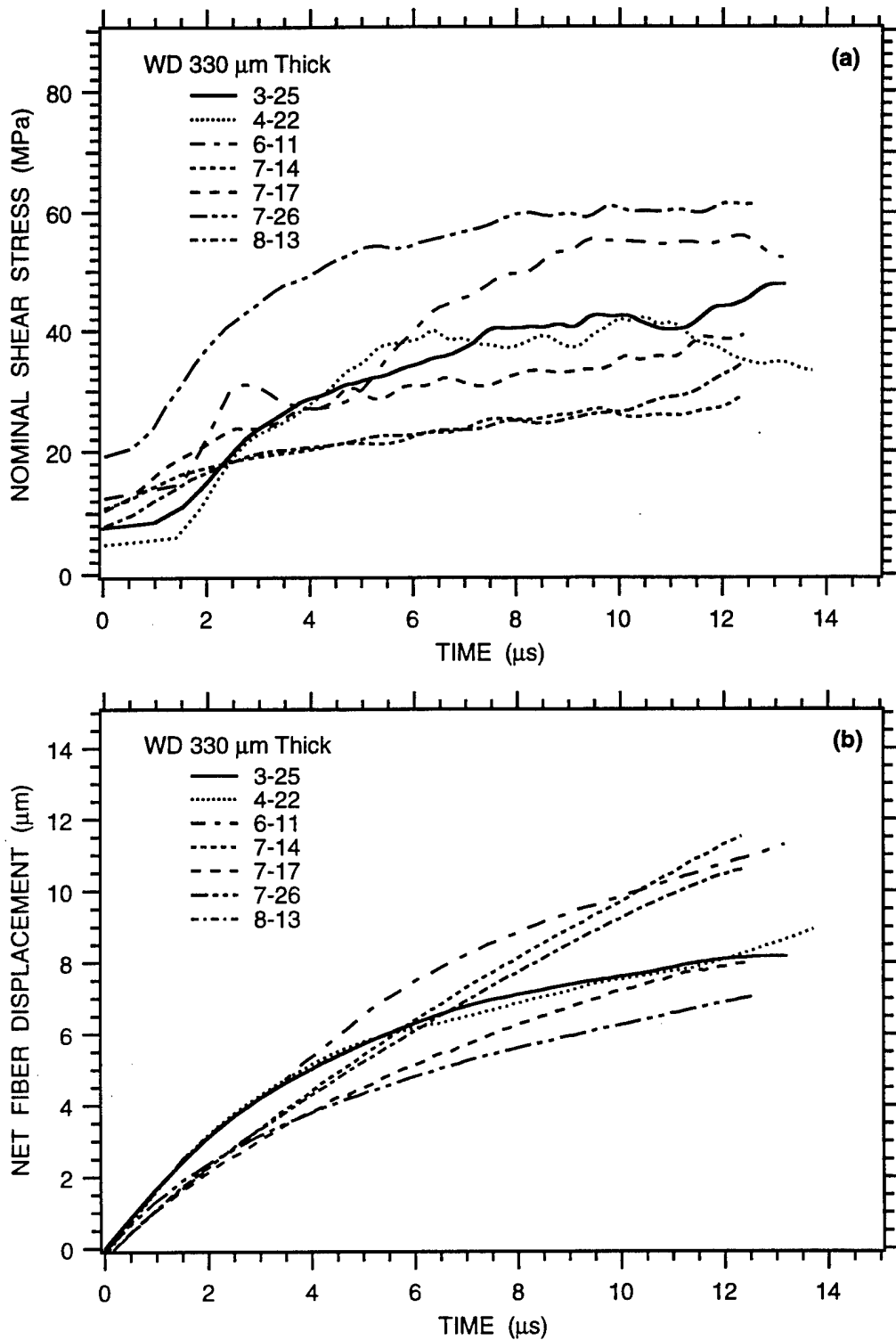
CAM-3311-54

Figure 7. Results of dynamic pushout experiments on 508-μm-thick specimens having SB microstructure.
3.3 m/s impact velocity.



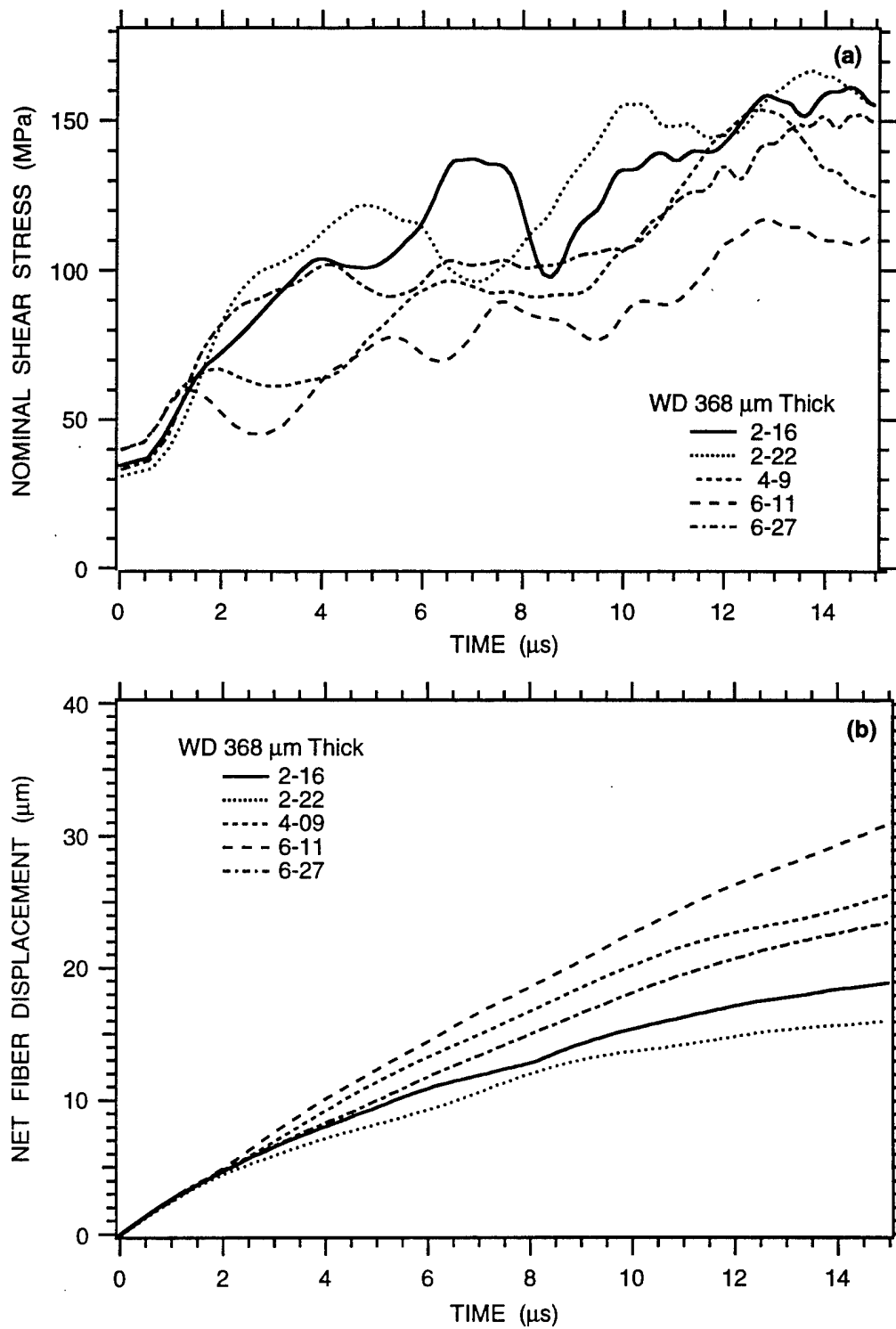
CAM-3311-55

Figure 8. Results of dynamic pushout experiments on 533-μm-thick specimens having SM microstructure.
3.2 m/s impact velocity.



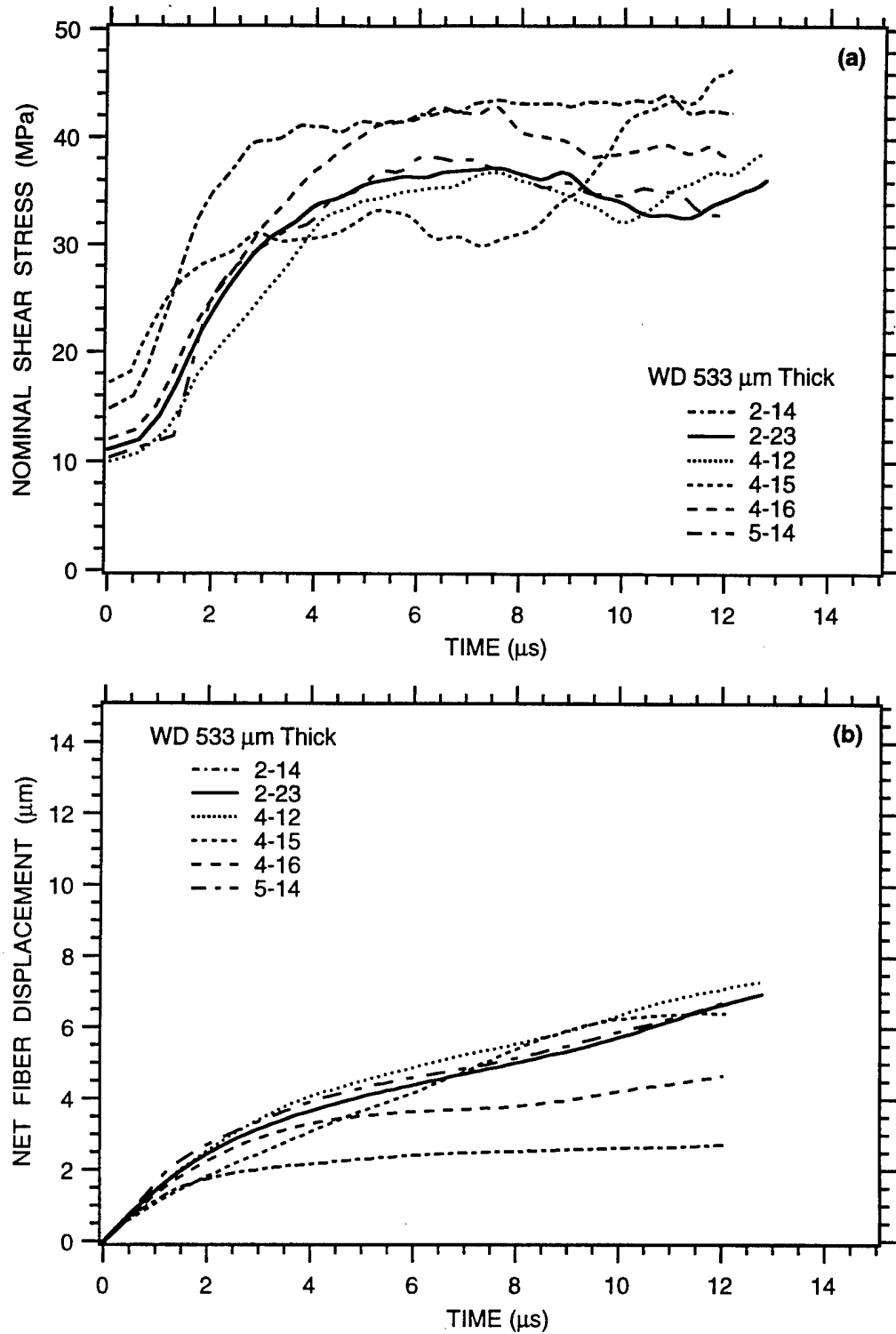
CAM-3311-56

Figure 9. Results of dynamic pushout experiments on 330-μm-thick specimens having WD microstructure.
1.9 m/s impact velocity.



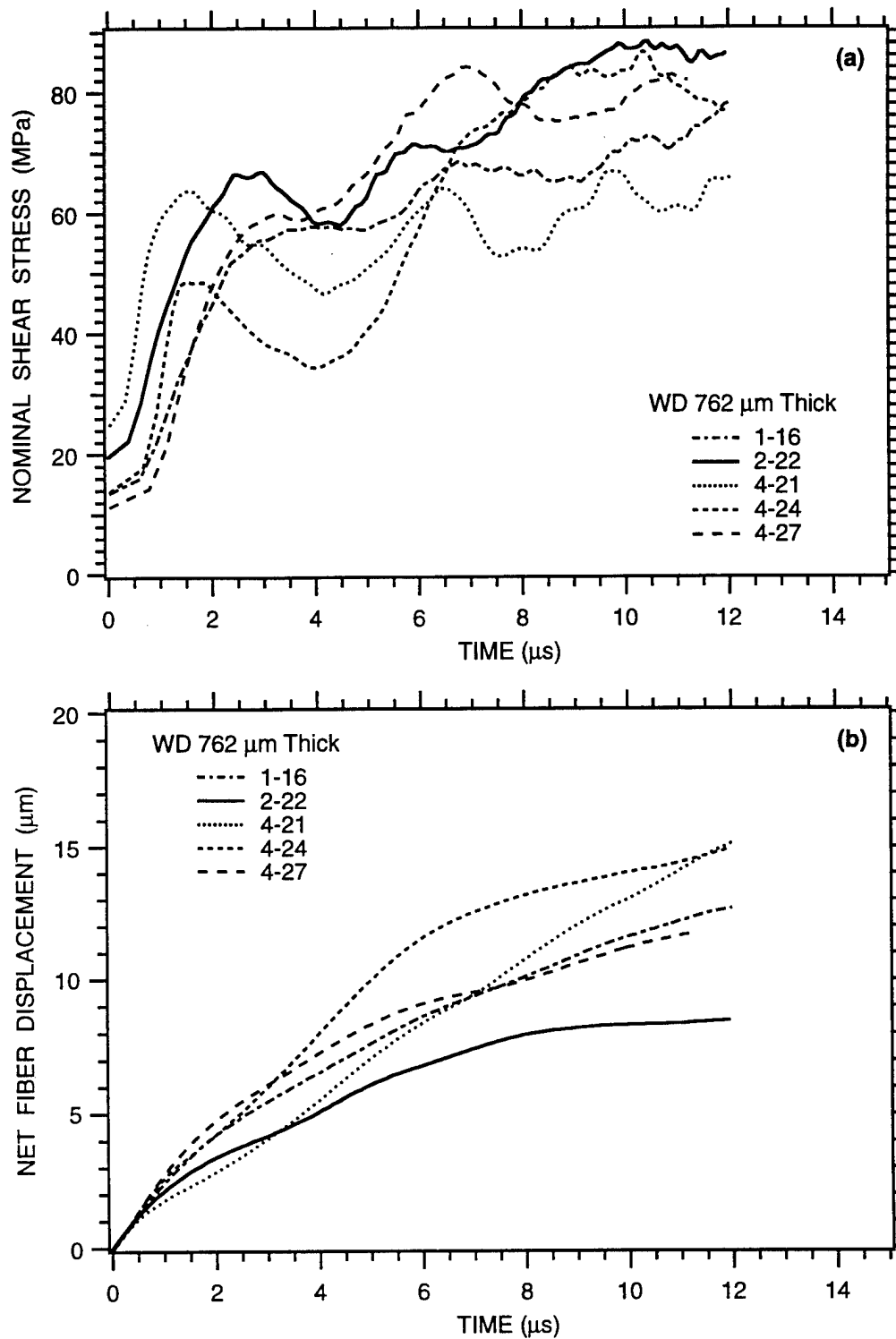
CAM-3311-57

Figure 10. Results of dynamic pushout experiments on 368- μ m-thick specimens having WD microstructure. 3.2 m/s impact velocity.



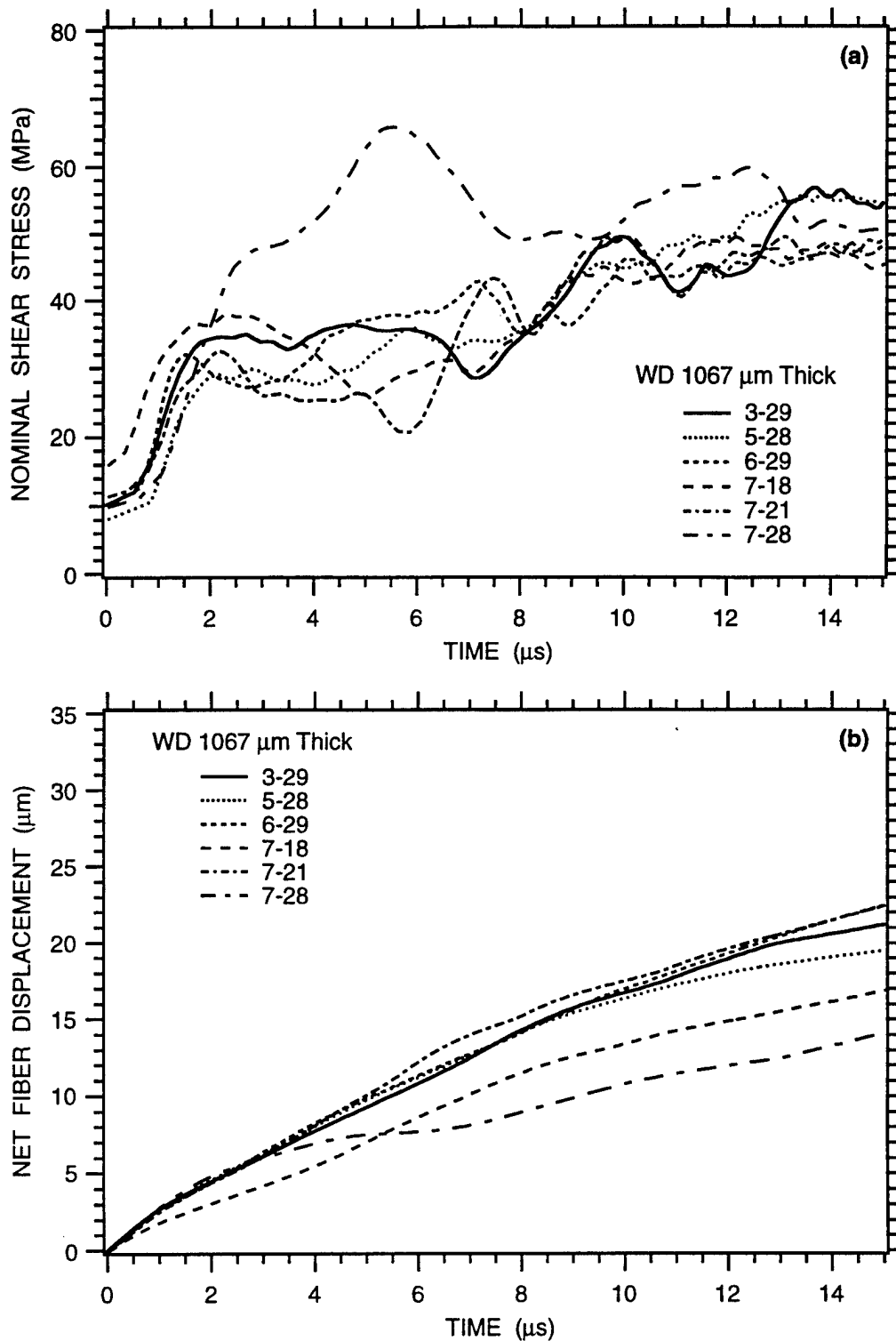
CAM-3311-58

Figure 11. Results of dynamic pushout experiments on 533- μ m-thick specimens having WD microstructure.
1.8 m/s impact velocity.



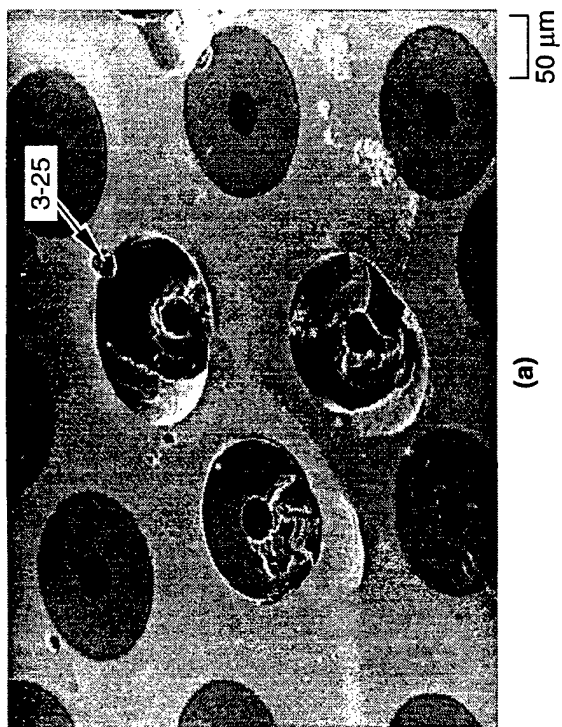
CAM-3311-59

Figure 12. Results of dynamic pushout experiments on 762- μ m-thick specimens having WD microstructure.
3.1 m/s impact velocity.

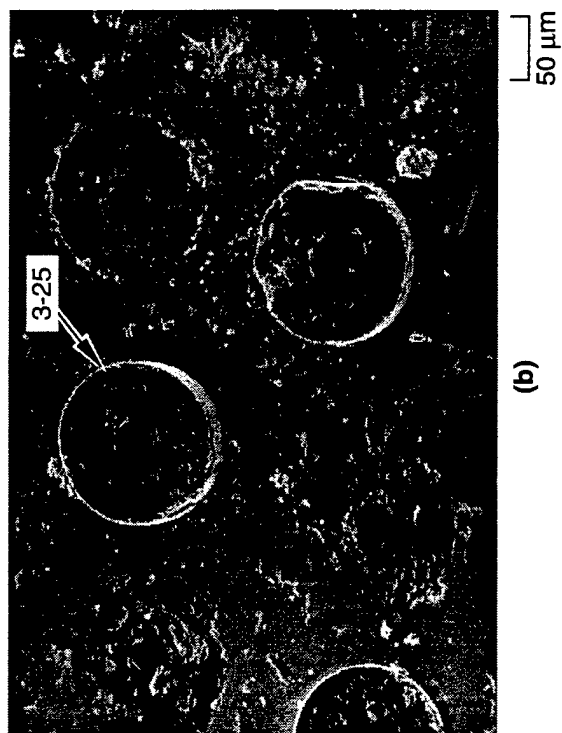


CAM-3311-60

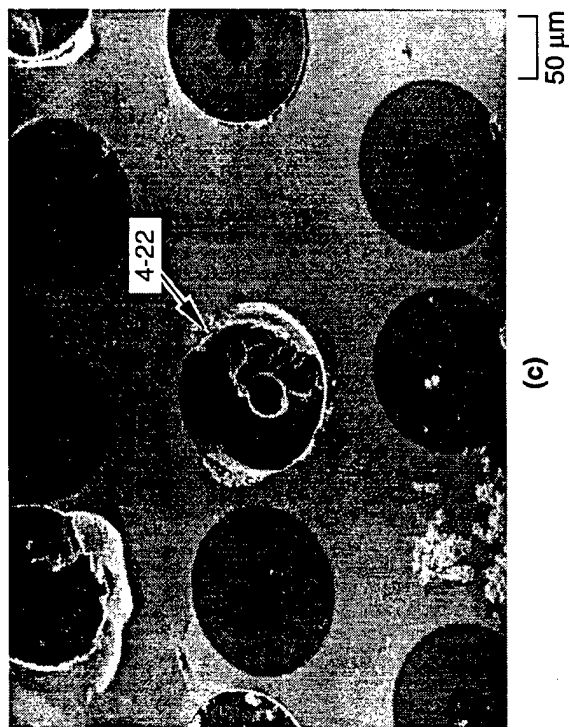
Figure 13. Results of dynamic pushout experiments on 1067-μm-thick specimens having WD microstructure.
3.2 m/s impact velocity.



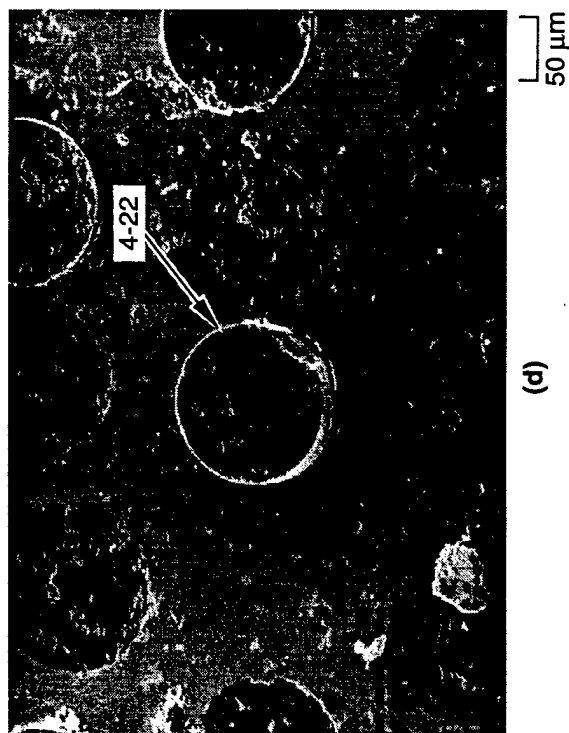
(a)



(b)



(c)



(d)

CPM-3311-21

Figure 14. Proximal and distal ends of impacted fibers.
WD microstructure, 330-μm thick, 1.9 m/s impact velocity.
(a) and (b) Test 3-25, (c) and (d) Test 4-22.

Table 1
SUMMARY OF PUSHOUT EXPERIMENTS

Micro-structure	Thick-ness (μm)	Number of Tests	Impact Velocity (m/s)	Nominal Shear Stress* (MPa)	Net Fiber Displacement* (μm)	Displacement Rate* (m/s)
SB	508	6	3.32 ± 0.06	128 ± 21	11 ± 6	0.47 ± 0.28
SM	533	4	3.16 ± 0.06	65 ± 4	8 ± 2	0.44 ± 0.23
WD	330	7	1.86 ± 0.05	41 ± 20	8 ± 2	0.46 ± 0.33
WD	368	5	3.22 ± 0.21	119 ± 37	18 ± 5	1.30 ± 0.60
WD	533	6	1.84 ± 0.04	38 ± 6	5 ± 3	0.30 ± 0.24
WD	762	4	3.12 ± 0.11	77 ± 12	12 ± 3	0.54 ± 0.53
WD	1067	6	3.16 ± 0.24	48 ± 5	15 ± 5	1.00 ± 0.40

* Mean over all tests of the value at 10 μs.

The mean shear stress results show some discernible trends. For the WD microstructure, at 3.2 m/s impact velocity, the mean shear stress decreases with increasing thickness: 368 μm thickness requires 119 MPa shear stress, 762 μm thickness requires 77 MPa, and 1067 μm thickness requires 48 MPa to push out the fibers. For the WD microstructure, at 1.8 m/s impact velocity, 330 μm thickness requires 41 MPa, whereas 533 μm thickness requires 38 MPa. (Note, however, the large stress variation in the 330-μm tests.) For similar thicknesses of 330 and 368 μm, the shear stress increases from 41 to 119 MPa as the impact velocity is increased from 1.9 to 3.2 m/s. The SB microstructure impacted at 3 m/s requires significantly greater (128 MPa) shear stress to push out the fibers than does SM microstructure (65 MPa) for impacts on similar-thickness slices. We have no direct comparison between WD and SB or WD and SM, because the impact velocity was 1.8 m/s in WD tests at 533 μm thickness. However, if we interpolate the 3 m/s WD values at 368 μm and 762 μm, we obtain a value for WD of 101 MPa.

Lerch¹² performed static pushout tests on ≈300-μm-thick slices of WD material. The pushout velocity was a few micrometers per second, about six orders of magnitude slower than in our pushout tests. Statically, the nominal shear stress rises sharply to 101 ± 17 MPa, then suddenly drops to 81 ± 16 MPa before rising again to a plateau of 126 ± 23 MPa. The

corresponding amount of pushout is similar to that in the dynamic tests, that is, a few tenths of fiber radii. The rise and drop in the shear stress are caused by the initiation and propagation of a debond crack and the plateau represents steady sliding.

Comparing Lerch's results and the dynamic results from slices 330 μm thick impacted at 1.86 m/s, the dynamic pushout stress is roughly one-third the peak static pushout force. On the other hand, comparing Lerch's results with results from slices 368 μm -thick impacted at 3.22 m/s, the dynamic force is roughly the same. End effects dominate the dynamic shear stress values we report and the static values Lerch reports,¹² because the dynamic pushout slices $\approx 300\text{-}\mu\text{m}$ -thick are only about four fiber radii thick. Thus, neither the static nor dynamic pushout stresses should be compared directly with data from thicker slices. Nevertheless, Lerch's static results and our dynamic results are comparable because the slices have similar thickness.

Shetty (see Dollar and Steif¹³) has analyzed the pushout experiment, using a shear lag model with Coulomb friction to determine the end effects on the pushout stress. Application of Shetty's model to the WD shear stresses measured on slices 368, 762, and 1067 μm thick at 3 m/s shows essentially no difference between Shetty's model and a constant shear stress model. Therefore, both models predict that the shear stress is independent of thickness. The WD shear stresses for slices 368, 762, and 1067 μm thick are respectively 119, 77, and 48 MPa, clearly not constant and clearly dependent on thickness. Therefore, neither model fits the dynamic data very well.

For the WD microstructure, the pushout resistance at constant thickness around 300 μm is 126 MPa at 2×10^{-6} m/s, 41 MPa at 1.8 m/s, and 119 MPa at 3.2 m/s. A possible explanation for the resistance at 1.8 m/s being lower than the resistance at 2×10^{-6} m/s or 3.2 m/s is that there is a difference in the mechanism that governs pushout resistance at quasistatic and dynamic rates. We believe that the behavior cannot be attributed to differences in the static and dynamic test techniques, since specimen thicknesses, support conditions, and load application area are essentially the same in both cases, and the tube-on-tube impact results (Figure 6) verify that the Hopkinson transducer is accurate.

For the WD microstructure, neither a shear lag model nor a constant shear stress model can explain why pushout resistance varies inversely with thickness at constant velocity. A candidate explanation for this behavior is that shearing resistance is not distributed uniformly throughout the thickness of the specimen. When stresses are averaged over the thickness, a thin specimen has a greater proportion of high-resistance region than a thick specimen and the average stress for the

thin specimen is therefore higher. We can only speculate on reasons for a nonuniform stress distribution.

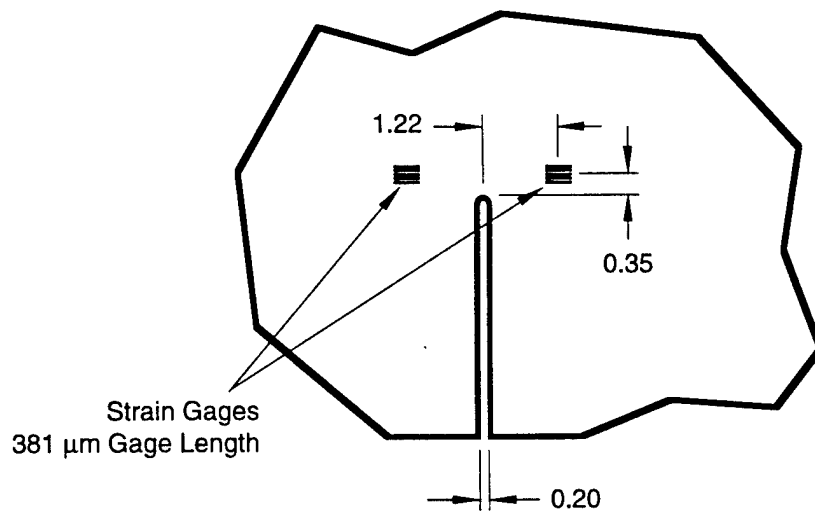
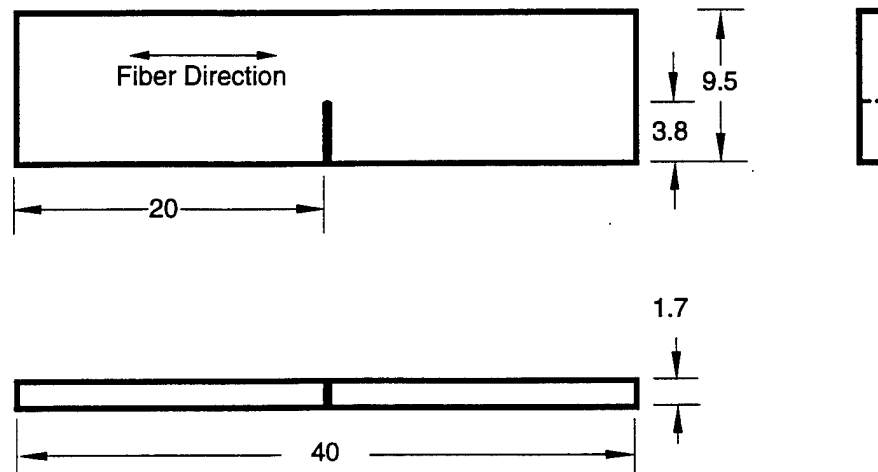
FRACTURE RESISTANCE MEASUREMENTS

Single-edge-notched bend bars of the WD, SM, SB, and Timetal® 21S composites were tested quasistatically and dynamically to determine the notch toughness and loading rate sensitivity in Mode I loading. Fibers were parallel to the long axis of the specimen, and perpendicular to the notch. Figure 15 shows specimen dimensions, which were the same for static and dynamic loading. For both types of loading, strains near the notch root were measured by strain gauges and recorded during the test.

Quasi-static toughness was determined in the three-point-bend tests performed using a servohydraulic testing machine at a loading rate of $0.2 \times 10^{-1} \text{ MPa}\sqrt{\text{m}}/\text{s}$. Load, strains, and AE were recorded. The notch root stress intensity was calculated from the load (the formulas relating load and geometry to the stress intensity are identical in the isotropic and orthotropic cases) and from the strains, using the plane stress singularity solution for an orthotropic material.¹⁴ To facilitate comparison with results of dynamic tests, all comparisons are made on the (common) basis of stress intensities derived from strains, rather than loads, because loads were not measured in the dynamic tests.

Two AE transducers were coupled to the sides of the static specimens to listen for the acoustic signals emitted by failure events occurring inside the specimen. Acoustic signals from failure events are recorded as hits when they arrive at the transducers and if they are of sufficient amplitude. For each of the three microstructures, a sudden increase in the number of hits per unit time occurred, indicating the onset of significant internal damage.

Dynamic fracture toughness was measured in one-point-bend impact tests performed using a small pneumatic launcher to accelerate a loading tup into the specimen. Impact velocities were around 30 m/s and loading rates were around $1.2 \times 10^7 \text{ s}^{-1}$. The one-point-bend test is fully described by Giovanola.^{15,16} Briefly, specimens are loaded with a tup, as in a three-point-bend test, but the outside supports are eliminated. The inertia of the specimen extremities provides the load reaction and the specimen bends, resulting in a smoothly increasing stress intensity history (up until fracture, if it occurs). The amplitude of the applied stress intensity at a given time after impact scales with the velocity, but the time to the peak stress intensity (providing fracture does not occur) is invariant because the time scale is governed by the natural frequency of the specimen.



Notch and Strain Gage Detail

CAM-3311-6

Figure 15. Three-point- and one-point-bend specimens.
(Dimensions in millimeters)

Figures 16 and 17 show stress intensity histories for WD, SM, SB, and Timetal 21S for the static and dynamic cases. Table 2 lists the toughnesses, taken to be the stress intensity at the first departure from linearity in the quasi-static case and the first departure from the scaled reference curve in the dynamic case. The toughnesses are designated K_{IQ} in Figures 16 and 17.

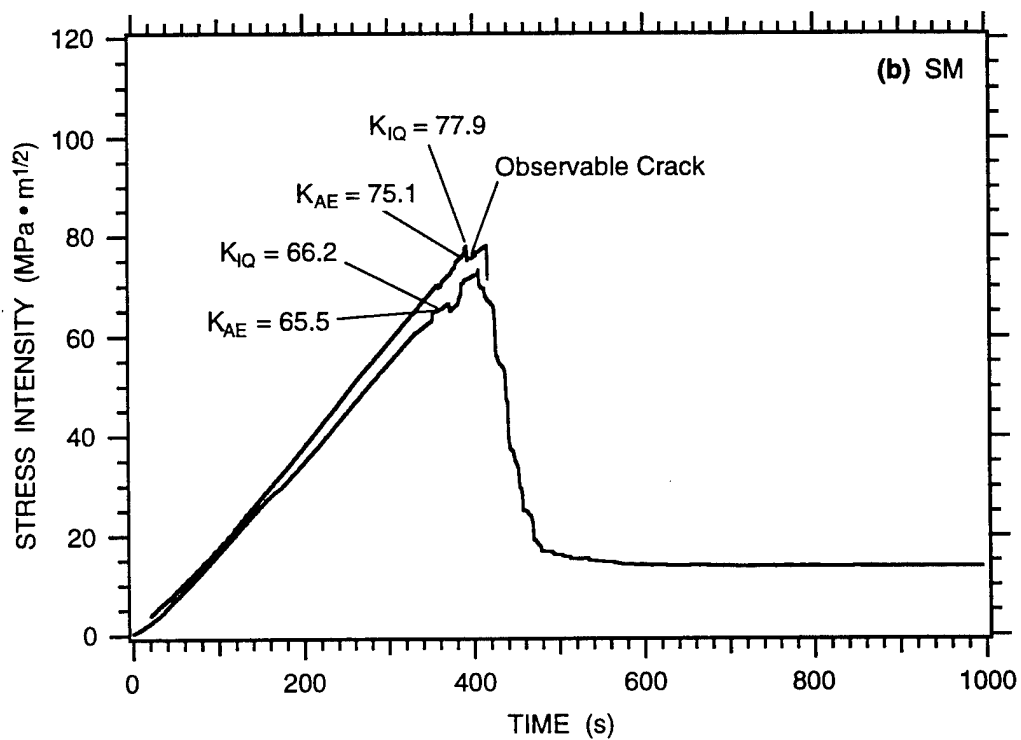
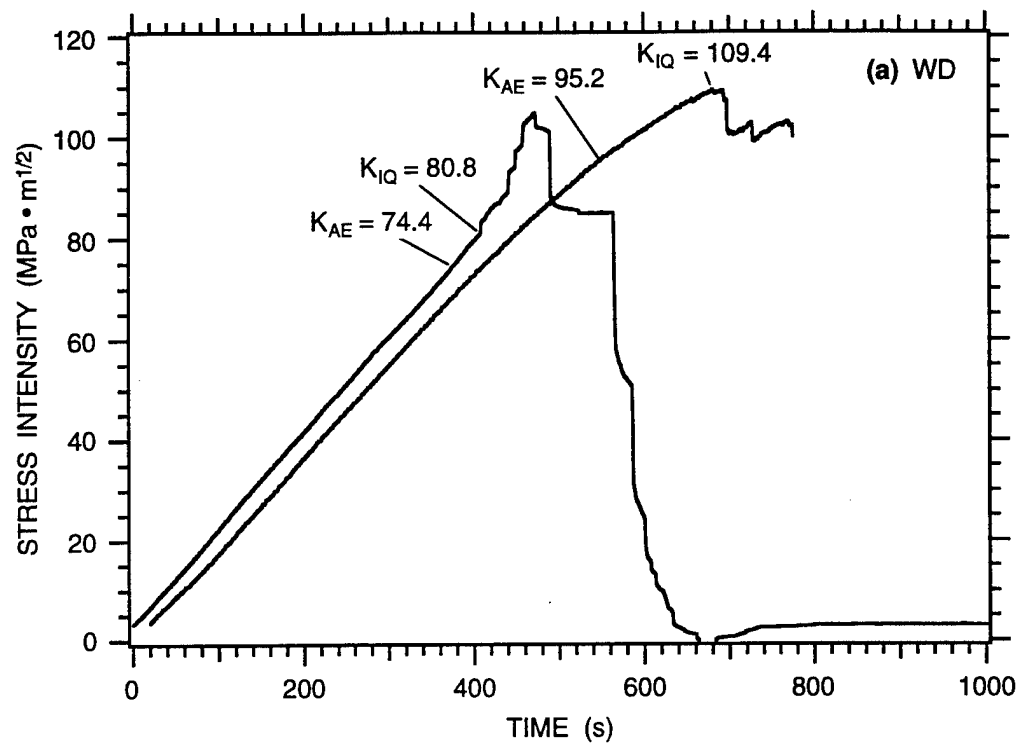
Table 2
RESULTS OF TOUGHNESS MEASUREMENTS

Heat Treatment	Ultimate Strength [1] MPa	Quasi-Static		Dynamic	
		Toughness MPa \sqrt{m}	Loading Rate MPa \sqrt{m} /s	Toughness MPa \sqrt{m}	Loading Rate MPa \sqrt{m} /s
WD	1455	80.8	1.8×10^{-1}	87.1	1.3×10^7
SB	1968	38.8	2.0×10^{-1}	71.1	1.0×10^7
SM	1706	66.2	2.0×10^{-1}	86.2	1.2×10^7
β 21S	1500*	42.7	2.0×10^{-1}	50.5	6.5×10^6

*Estimate from rule-of-mixtures theory.

Table 2 shows that, except for the SB microstructure, the toughness of the composites is moderately sensitive to loading rate. The SB microstructure is particularly sensitive; the toughness increases by a factor of 1.8 over an 8-decade increase in loading rate. Except for the SB static case, the toughnesses are similar to those obtained for plane strain specimens of the unreinforced, near-beta alloy Ti-10-2-3 ($55\text{--}75 \text{ MPa}\sqrt{m}$).¹⁷

Cursory examination of the specimens showed typical mode I failure and minor fiber pullout in all cases except the SB static case. In that case, the crack initiated and grew at a large angle (60°) with respect to the notch, suggesting that low resistance to matrix fracture parallel to the fibers dominated the failure response. In the SB dynamic case, the crack grew in the plane of the notch, although the extent of fiber pullout seemed to be less than that in the WD and SM cases. Indeed, we found in the dynamic fiber pushout experiments that the SB microstructure had the strongest fiber-to-matrix bond.

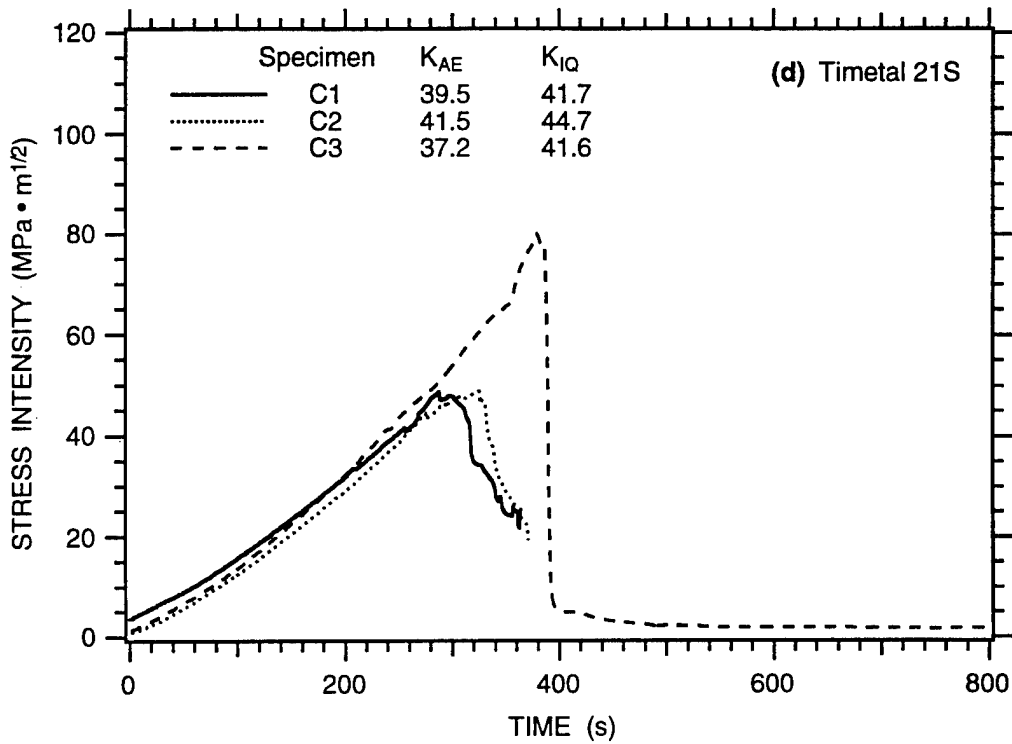
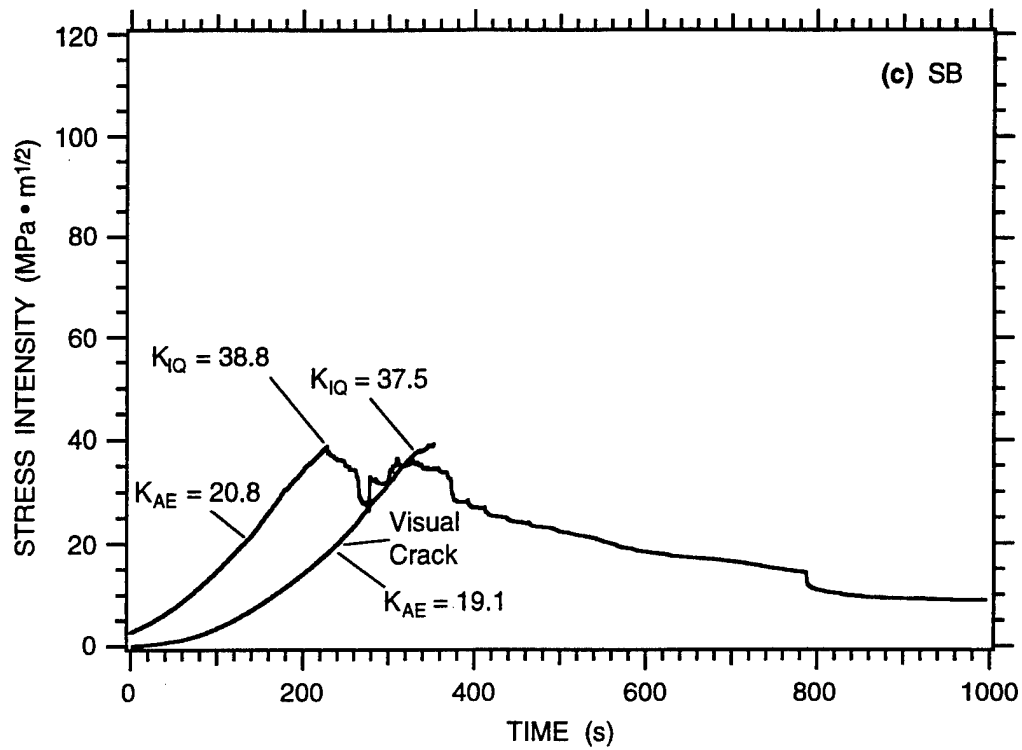


CAM-3311-61

Figure 16. Quasistatic 3-point bend test results for various microstructures.

Data from each of two tests is provided to show reproducibility.

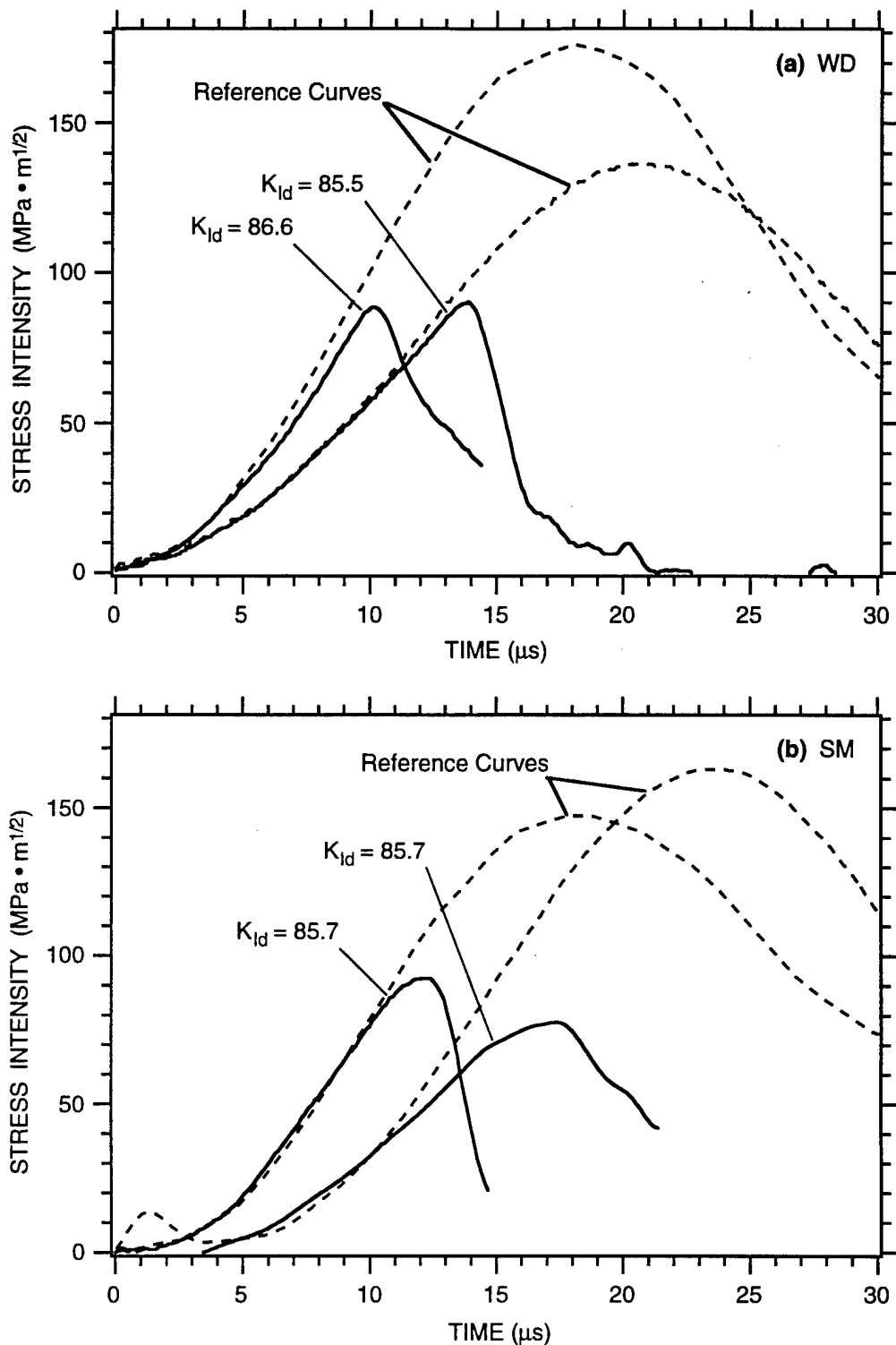
(Continued)



CAM-3311-62

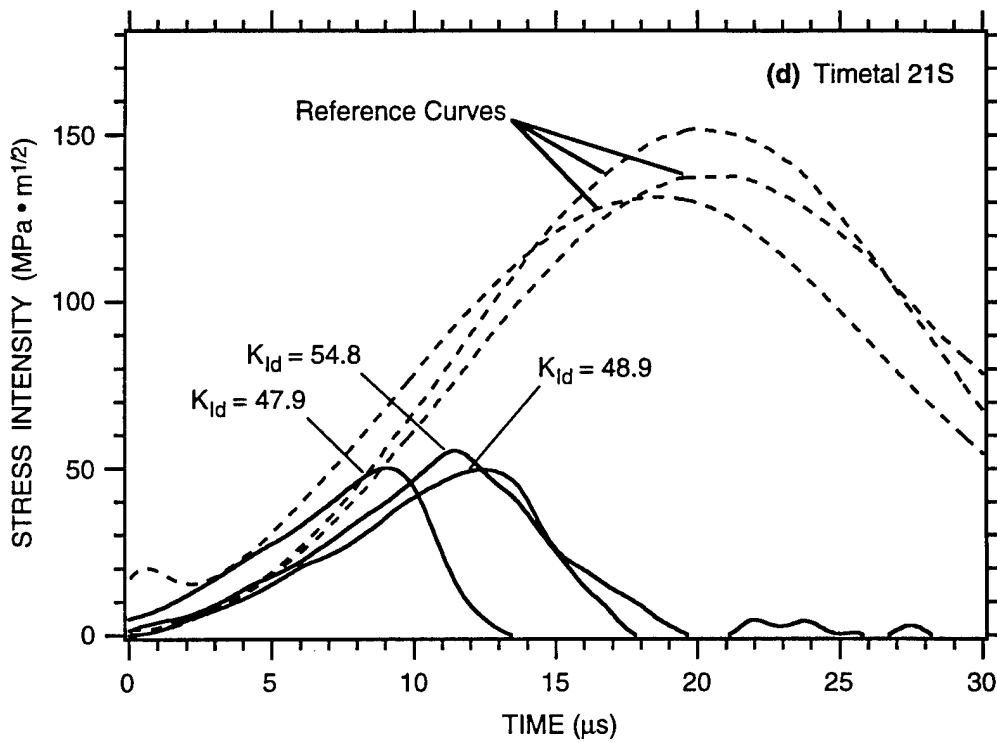
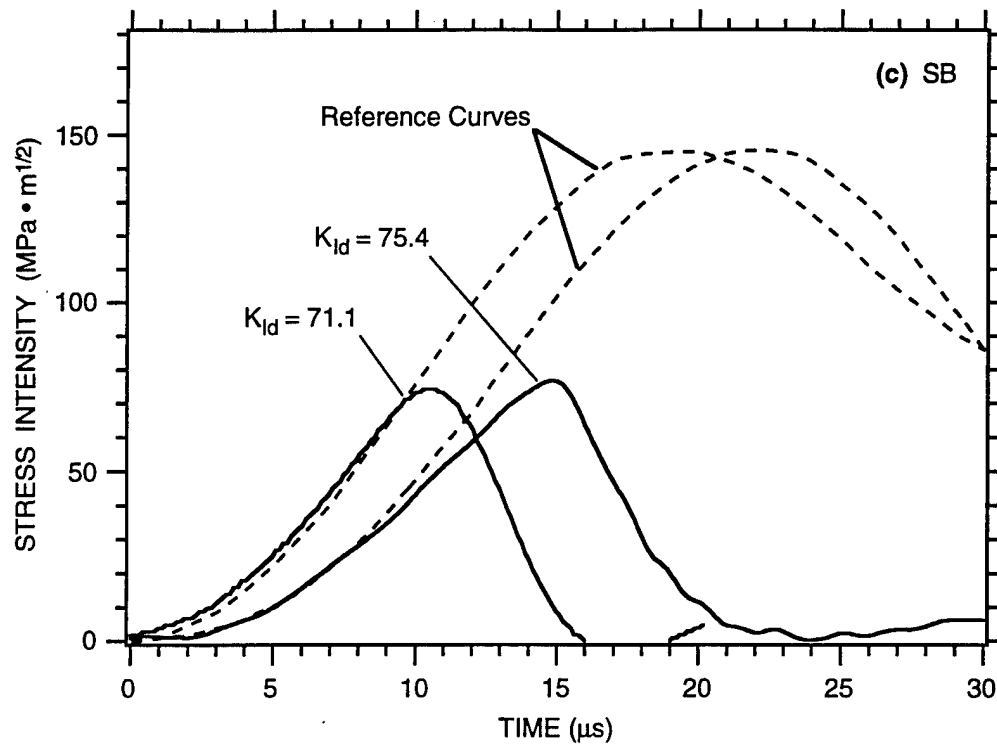
Figure 16. Quasistatic 3-point bend test results for various microstructures.

Data from multiple tests is provided to show reproducibility.
(Concluded)



CAM-3311-63

Figure 17. Dynamic one-point bend test results for various microstructures.
Data from each of two tests is provided to show reproducibility.
(Continued)



CAM-3311-64

Figure 17. Dynamic one-point bend test results for various microstructures.
Data from each of two tests is provided to show reproducibility.
(Concluded)

In the quasi-static tests, except for the SB microstructure, a sudden increase in AE occurred just before the strain records departed from linearity, taken to signify macroscopic fracture initiation. For the SB microstructure, significant AE began at about half the macroscopic fracture initiation load, yet there was no identifiable correlated feature on the stress intensity history.

The Timetal® 21S MMC is less tough than the Ti-15-3 MMCs, but the general trend that the dynamic toughness is 10%-30% higher than the static toughness mirrors the behavior of the WD and SM Ti-15-3 MMCs.

In summary, the toughness of three of the MMCs is similar to that of unreinforced titanium alloys. The toughnesses of the WD, SM, and Timetal® 21S microstructures, increase 9%, 30%, and 18%, respectively, over an 8-decade increase in loading rate. The toughness of the SB microstructure, on the other hand, increases by 80% and is accompanied by a change in fracture mode from Mode II to Mode I. Heat treatment clearly influences both the absolute toughness and the relative increase with loading rate. Microstructural examinations, summarized in the next section, suggest that the rate sensitivity in notched bending failure is governed by the rate sensitivity of the matrix metal and that the fibers and interfaces play a relatively small role.

MICROFAILURE CHARACTERIZATION

Figures 18-21 show cross sections of the notch root regions of one-point- and three-point-bend specimens for the WD, SM, and Timetal® 21S microstructures. Cross sections of the other microstructures, both statically and dynamically loaded, show similar features. The cross sections were prepared by planar grinding and polishing parallel to the specimen faces. Some pieces of fiber are clearly missing, having probably fallen out during the grinding process. In all cases, fiber failure clearly precedes matrix failure. Fiber failure occurs at multiple locations both on and off the main crack path. There appears to be little evidence of any sort of fiber bridging helping to knit the matrix together, as shown, for example, in the micrographs of Ti-15-3 specimens loaded in tension shown by Majundar, et al.¹⁸

For our bend specimens, secondary fiber fractures located off the main crack line typically are connected to the main crack by debond cracks, which occur between reaction zone and coating layers and extend along the fibers between the fiber fracture locations. At a few of these secondary fiber fracture locations, a short crack extends through the reaction zone layer and into the matrix. We cannot rule out the possibility that these secondary cracks formed during sectioning.¹⁹

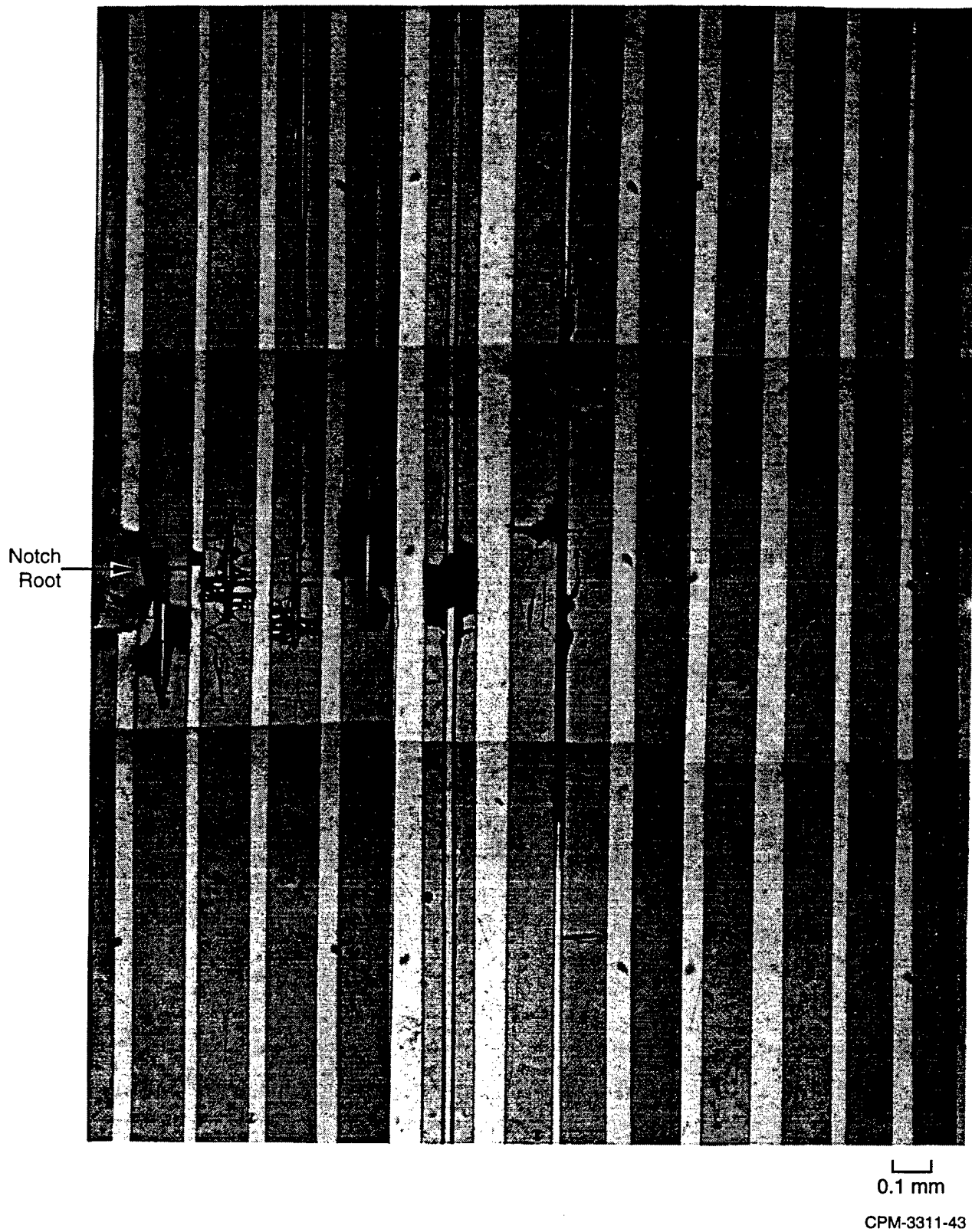
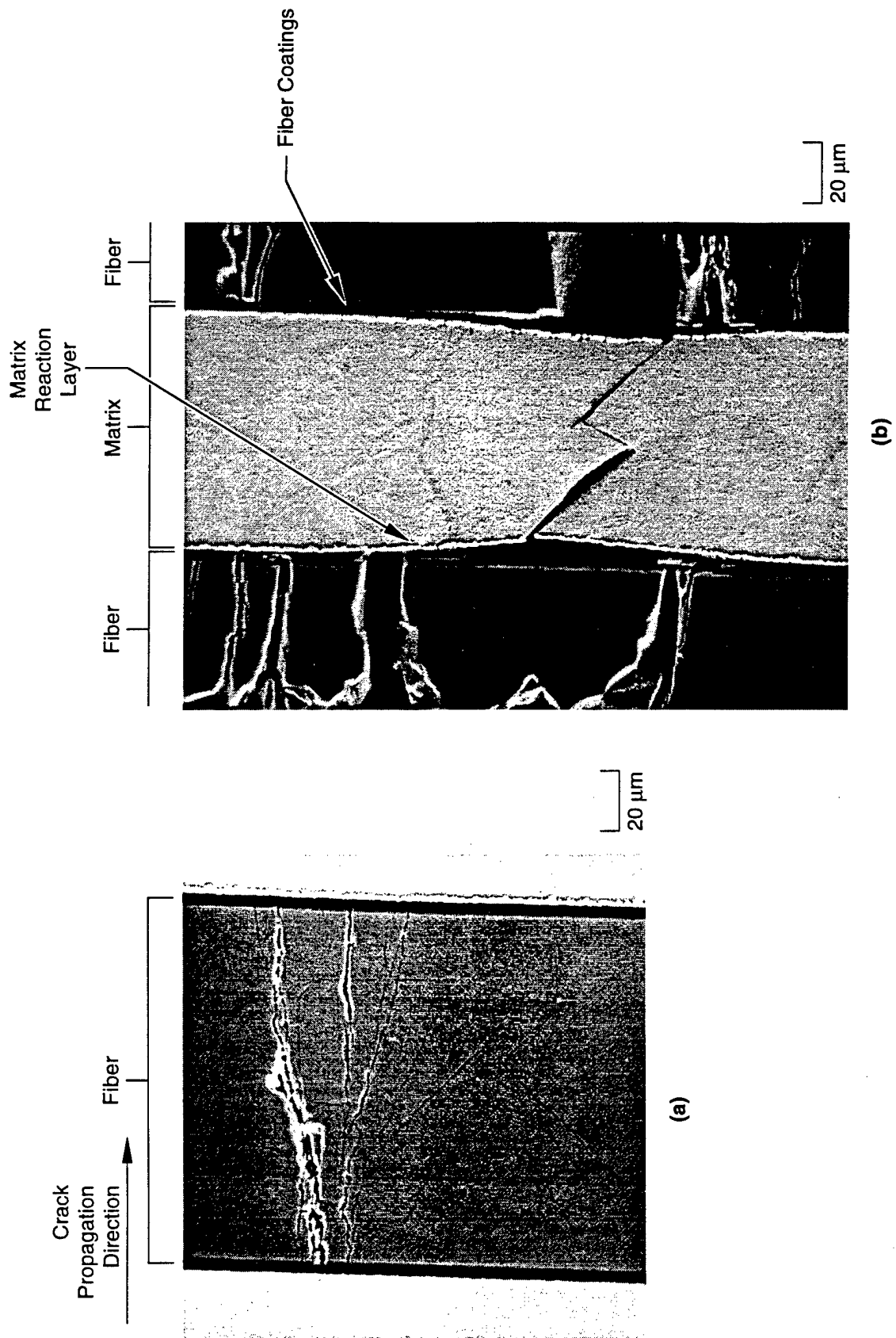


Figure 18. Cross section of the crack line region of the WD microstructure, dynamically loaded.



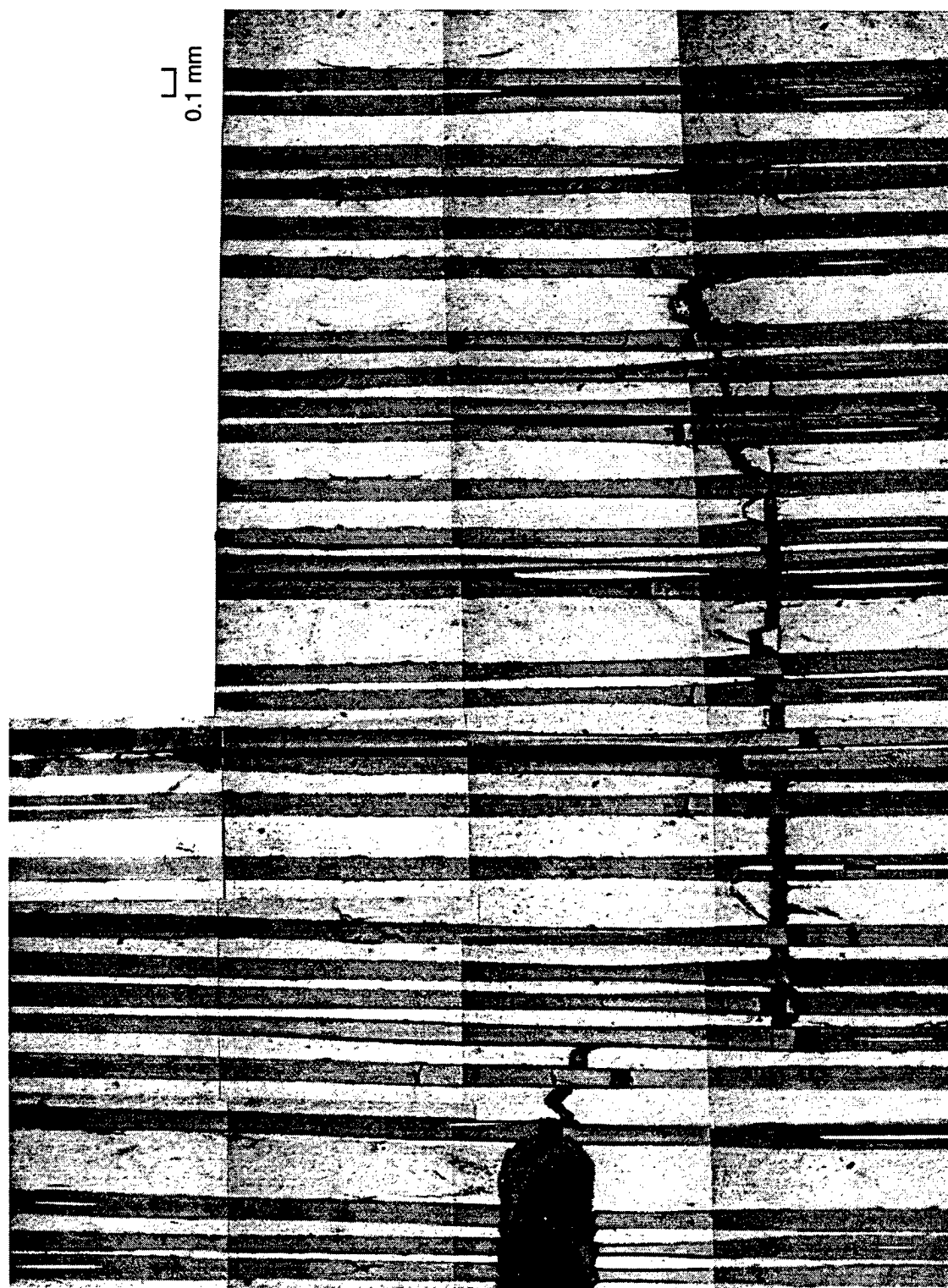
CPM-3311-41

Figure 19. Cross section of the crack line region of the SM microstructure, statically loaded.



CPM-3311-52

Figure 20. Ti-15-3 SM microstructure failure phenomena.



CPM-3311-42

Figure 21. Cross section of the crack line region of the sigma-fiber/TIMETAL 21S microstructure, statically loaded.

The matrix material between the fibers is typically debonded from the adjacent fibers and has necked in areas near the adjacent primary fiber fractures (see Figure 20b). The matrix cracks along $\approx 45^\circ$ planes in the necked regions. In the debonded and necked regions, the matrix debonds along the interface between the matrix reaction layer and the carbon-rich layer coating the fibers. The reaction layer remains attached to the matrix, while the carbon-rich layers follow the fiber. The debond crack is not restricted to the necked region, but rather extends away from the main crack by as many as 5 fiber diameters. This debond crack follows the interface between the carbide layer and the first carbon-rich layer and extends along a continuous unfractured fiber until terminating.

In many instances, primary fiber fractures have a distinct river-delta pattern like that shown in Figure 20a. The patterns fan out in the direction of crack propagation and suggest that the fractures formed in bending. Micrographs of Ti-15-3 MMC loaded in axial tension, without bending, do not exhibit these fracture patterns (see Lerch and Saltsman²⁰).

The microstructure of the Sigma fiber/Timetal 21S MMC contains distinct matrix regions of two widely different grain sizes, which become apparent upon etching. There are fine-grained tow ribbons woven imprecisely between the fibers. The remaining matrix has a much larger grain size and is separated from the tow ribbons by a sharp interface. Fracture sometimes follows the interface between the fine and coarse grained regions.

The tow wires used to align the SiC fibers strongly influenced the fracture path when the wires were within a millimeter or so of the notch root. In these cases, fractures would typically initiate at the notch root and run perpendicular to the notch, parallel to the fiber direction. At the tow wire, the crack would turn perpendicular to the fiber direction across the reaction zone layers and run along the tow wire.

In summary,

- Fiber fractures lead matrix cracking by several fibers.
- Fractures on each fiber can occur at more than one location along the fiber.
- The presence of tow wires (Ti-15-3) and fine-grained tow ribbons of titanium (Timetal[®] 21S) influences where fracture occurs.

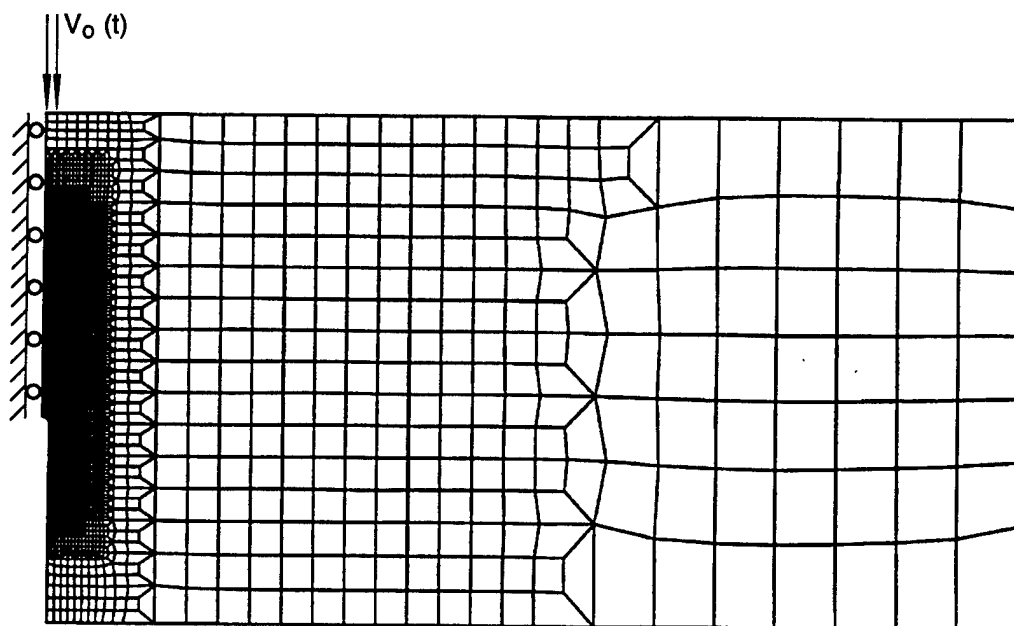
MODELING

The micrographs of fracture process zones (e.g., Figures 18-21) show that fracture develops over a region of at most a dozen fiber spacings in extent, and the gradation in damage from one fiber location to the next is significant. Thus, models that attempt to "smear out" the fibers, matrix, and interfaces in the process zone into an equivalent continuum would seem to provide insufficient fidelity for the purpose of designing materials. Thus, we developed a finite element model in which matrix, fibers, and interfaces are treated explicitly in the vicinity of the crack tip and are averaged only remotely, where deformations are negligibly small.

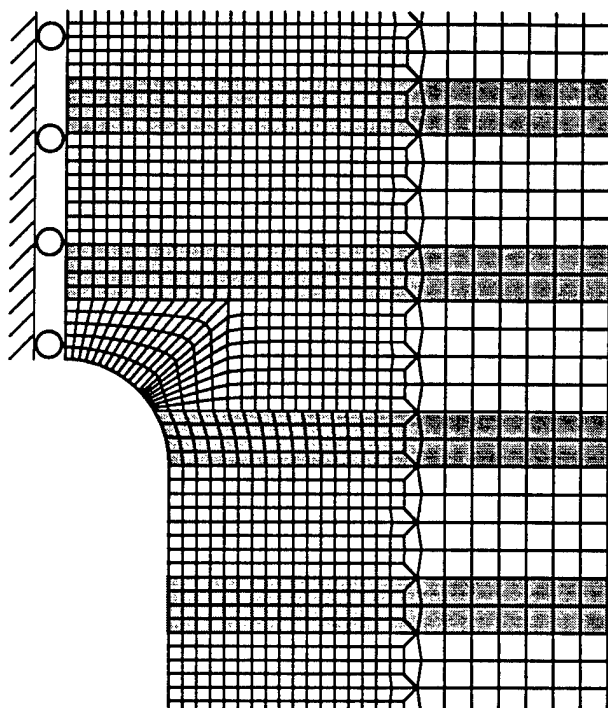
We used the dynamic, explicit, two-dimensional, finite element code DYNA2D²¹ to model the three-point-bend test configuration in plane strain. Figure 22 shows the mesh. Because the problem is symmetric, only half of the specimen had to be modeled. The mesh is composed of an outer, homogenized region modeled as an isotropic, elastic, perfectly plastic material surrounding a core crack line region composed of alternating layers of titanium alloy modeled as elastic perfectly plastic and silicon carbide modeled as elastic strain-hardening plastic with a maximum principal normal stress cutoff. When the maximum principal normal stress exceeds a threshold, deviatoric stresses are set to zero, and no hydrostatic tension is permitted. The cutoff stress is less than the yield stress so that, in tension, the SiC is an elastic material with brittle failure.

The properties of the homogenized material²² were used under the assumption that the longitudinal properties applied isotropically. Clearly, the outer region in the real composite is not isotropic, but deformations there are very small, occur largely in the longitudinal direction for which the moduli are correct, and are elastic. Table 3 gives baseline material model parameters for the homogenized region, the titanium, and the SiC. Those parameters not used in the model are left blank, even though they may be known.

Fiber-matrix interfaces in the core region were modeled using slidelines built into the finite element mesh. The slidelines used a Coulomb friction model for the interface shear stress and used a penalty formulation to prevent interpenetration of nodes on either side of the slideline. Slidelines were permitted to freely separate. The friction coefficient was 0.2. The MAZE²³ input file for DYNA2D is presented in the Appendix.



(a) Overall view, with core region shaded black



(b) Notch root vicinity, with fibers shaded gray

CM-3311-47

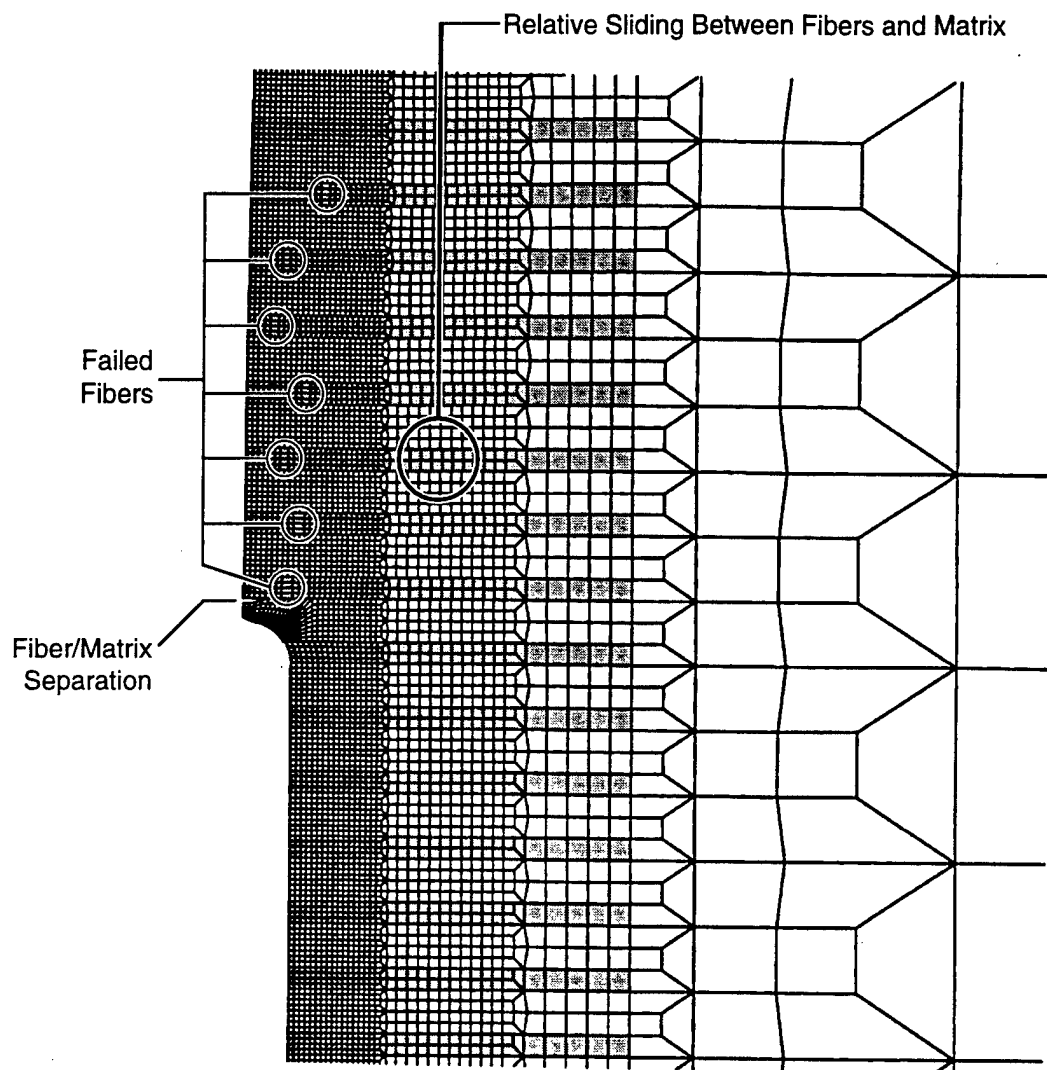
Figure 22. Finite element mesh.

Table 3
MATERIAL PROPERTIES FOR THE FINITE ELEMENT MODEL

	<u>Units</u>	<u>Homogenized</u>	<u>Ti-15-3</u>	<u>SiC</u>
Density	kg/m ³	3617	4650	3100
Young's modulus	GPa	203	82	
Shear modulus	GPa			160
Poisson's ratio		0.27	0.32	
Yield stress	GPa	1.455	0.876	10.0
Tangent modulus	GPa	0	0	400
Cutoff stress	GPa			2.6

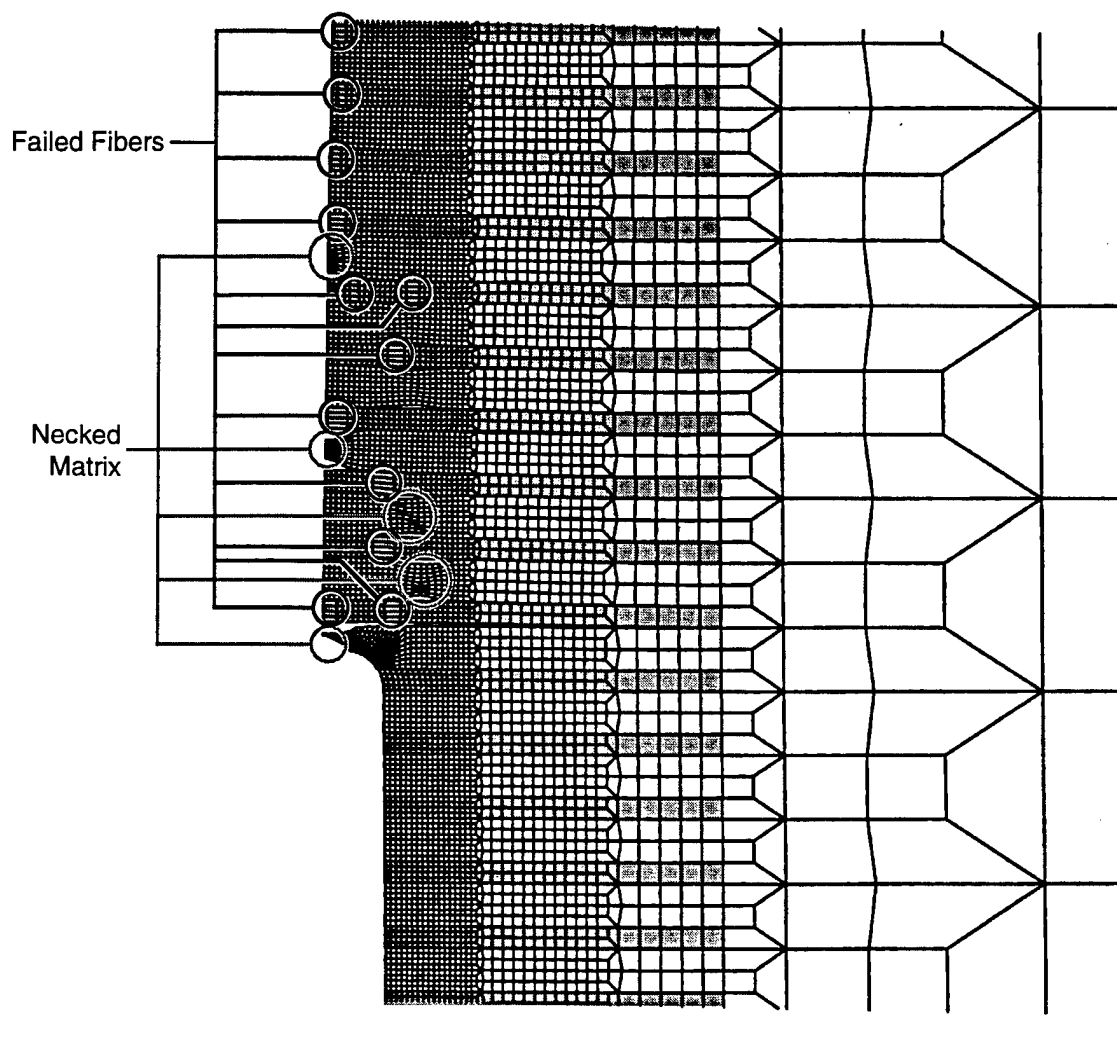
The boundary conditions were that nodes on the symmetry line be constrained of motion in the horizontal (x) direction and that the load be applied by imparting a velocity history to the two nodes on the impact edge of the specimen closest to the centerline, shown in Figure 22. The velocity history was a linear rise from 0 to 30 m/s over 1 μ s, remaining at 30 m/s thereafter.

Figures 23 and 24 show the deformed mesh. The locations of fiber failure are clearly visible as columns of distended elements. As in the experiments, the fiber failures occur at varying distances from the expected crack path. Matrix necking occurs immediately adjacent to the fiber failures, and is particularly evident at later times in the computation. Matrix and fibers separate from one another in the necked regions, and there is relative sliding between the two. The finite element problem is symmetric about the specimen centerline, and fiber failures and matrix necking therefore occur at mirror locations to the ones shown in Figures 23 and 24. Broken fiber segments would always bridge the main crack path. However, there is no reason for failures to actually develop at the mirror locations in a real loading; one side or the other will likely be favored and inhibit the development of the other. Furthermore, the finite element model never develops a matrix crack along the main path for the fiber segments to bridge. Thus, in agreement with the experiments, the finite element model predicts that fiber bridging plays only a small role in the failure of these MMCs in notch bending under monotonic loading. We performed a finite element



CM-3311-48

Figure 23. Deformed mesh at $t = 10 \mu s$. Failed fiber elements are distended and clearly visible.



CM-3311-49

Figure 24. Deformed mesh at $t = 18 \mu s$. Necking of titanium alloy has followed fiber failure.

calculation in which the matrix strength was reduced by a factor of 10, and similar behavior was observed.

Figure 25 compares measured strains from a one-point-bend experiment and computed strains from two finite calculations. For the case of $\sigma_y = 87.6$ MPa, the fibers fail quickly and the matrix strains readily because it is relatively soft. For the case of $\sigma_y = 876$ MPa, the fibers still fail quickly, but the matrix strains less because it is stronger. Although 876 MPa is the approximate yield strength of the matrix, the second finite element calculation suggests that the response is too stiff, and lies somewhere between the two cases. We have not investigated the effect of varying the fiber strength parameter.

SUMMARY OF RESULTS

The results of our research can be summarized as follows:

- The fracture resistance of these MMCs in notched bending increases by roughly 10%-30% as the loading rate increases from 10^{-1} to 10^7 MPa $\sqrt{\text{m}}$ s $^{-1}$ (roughly 10^{-7} m/s to 10^1 m/s in terms of the crack tip opening rate), which is similar to the amount that the fracture resistance of the matrix metal alone would be expected to rise. Thus, the dynamic effect on the toughness of these MMCs is moderate.
- Metallographic examinations of failed composites showed that fiber failure generally occurs on the crack line well ahead of the main crack, and fiber bridging is therefore mostly precluded. This early fiber failure frequently appears to have been induced by fiber bending. The lack of bridging fibers implies that pushout measurements, which are useful for understanding bridging phenomena, are not relevant in the case of significant bending.
- Examination of failed composites showed that the size of the fracture process region is on the order of 10 fiber spacings. Thus, fracture models that avoid taking explicit account of the constituents and their spatial arrangement (e.g., homogenization) might be inaccurate.
- A finite element model that does take explicit account of fibers, matrices, and interfaces indicates that fiber failure strains are exceeded in fibers well ahead of the main crack tip, and that these failures can be on or off the projected crack line. Matrix failure occurs adjacent to places in which fiber failure has already occurred, again suggesting that fiber bridging is generally precluded. The finite element model appears to reproduce the experimentally observed microfailure process.

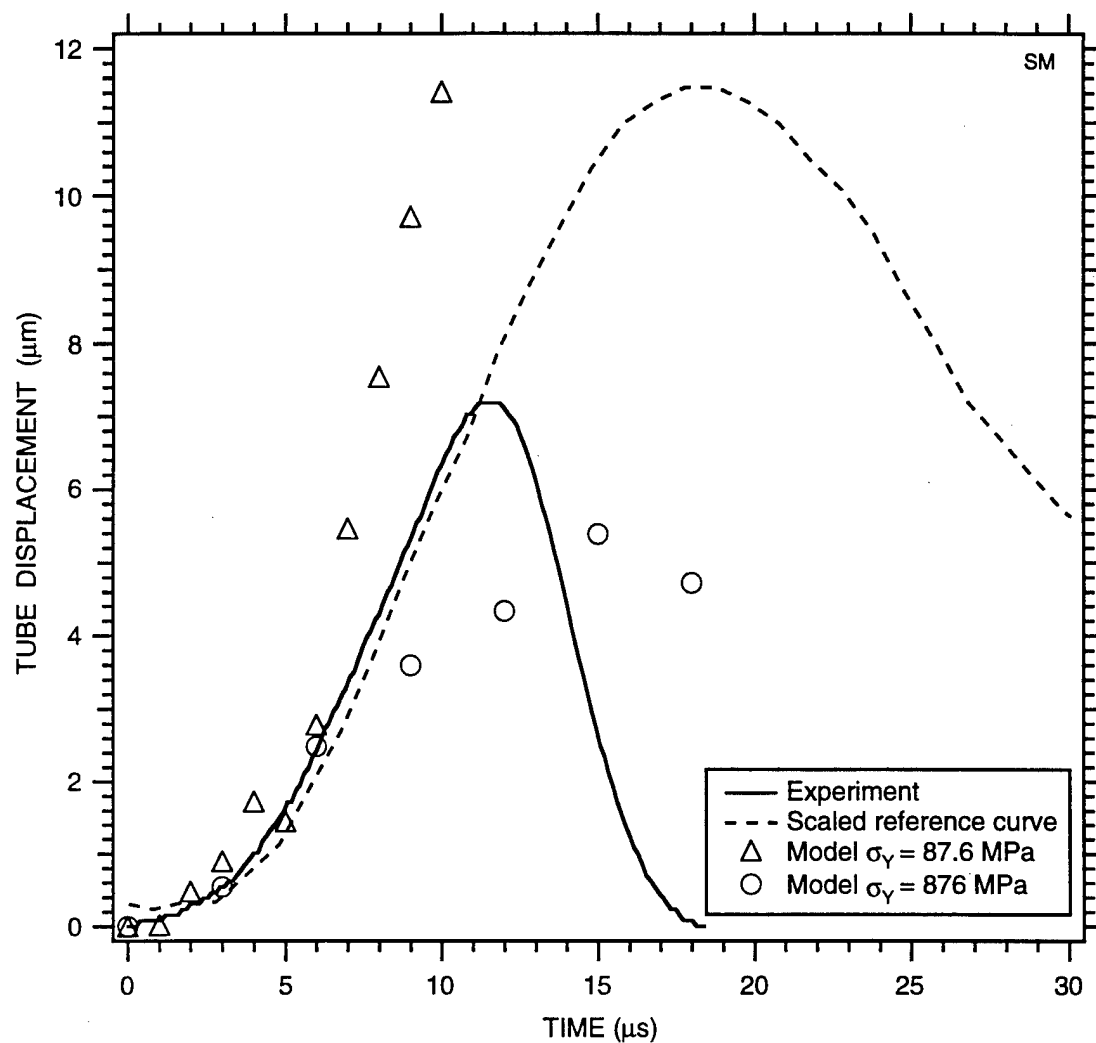


Figure 25. Comparison of strains from experiment and finite element model for SM microstructure.

Section 4

DISCUSSION AND RECOMMENDATIONS FOR FURTHER STUDIES

The notched bend fracture tests, microstructural examinations, and finite element modeling show that the matrix dominates the failure behavior of the MMCs, both statically and dynamically. Because the fibers are highly brittle relative to the matrix, the fibers fail well ahead of any matrix crack and therefore are unable to provide any toughness enhancement via bridging. These materials behave poorly where bending prevails. These observations suggest that aircraft parts fabricated from Ti-15-3 and Timetal® 21S MMCs would be susceptible to foreign object damage, at least at and below room temperature. Localized impacts which bend MMC parts are likely to break the interior fibers.

Fortunately, the dynamic effect on toughness is moderate and positive; toughness increases 10%-30% over an 8-decade increase in loading rate. The dynamic toughness of the MMCs is higher than the static toughness, is similar to unreinforced titanium alloy, and is in contrast to some materials (low carbon steels, for example) that undergo a ductile to brittle transition with increasingly dynamic loadings.

Because of the lack of bridging phenomena, the fiber pushout results are hardly applicable to the bending fracture of these MMCs. The pushout results may, however, apply in cases where bending is minimal (for example, in the axial loading of slender members). We suggest that the pushout results might be used to predict MMC fracture behavior in the absence of bending. Tests could then be performed using, for example, a panel in tension with a crack near the center to check the prediction, and the finite element model could be verified against the results and thereby be made available for cases in which bending plays a small role and bridging is active.

In the pushout tests, we noted a drop in nominal interface shear strength with decreasing interface length (i.e., slice thickness) and suggested that interface shear strength might be higher in some regions. This phenomenon must be understood if one wishes to understand and predict bridging. We suggest that microstructural examinations and finite element modeling be performed in an attempt to find the cause of the phenomenon. In particular, a finite element model including the pushout impactor might indicate whether fiber expansion under the impactor leads to increased pushout stress. Microscopy might reveal whether environmental attack from the surface or the act of preparing the slice leads to increased pushout stress near the surface.

Cross sections of the bend fracture specimens show that fiber failure precedes matrix failure. The AE data support that conclusion because significant AE also precedes composite failure in the bend tests. However, we did not confirm the source of the AE, which we presume to be brittle fiber failure. The FRASTA technique²⁴ might enable one to reconstruct the timing of microfailure events and identify the source of AE, although FRASTA fails when portions of fibers are lost posttest. Confirming AE with FRASTA would help ensure that the timing of microfailure events in the model coincided with the timing of microfailure events in the actual composite.

The parameter space of the finite element model remains mostly unexplored. The model appears to reproduce, at least qualitatively, brittle fiber failure, ductile matrix necking, and separation between fibers and matrix. We suggest that a parameter study be undertaken to predict, for example, the effect of variations in the interface friction coefficient on MMC failure. Other important parameters are the relative strains to failure of the matrix and fibers, matrix flow strength, fiber size and spacing, and the rate sensitivity of the matrix flow strength. Variations in the latter could corroborate the observation that the rate sensitivity of the matrix is largely responsible for the rate sensitivity of the composite. The model could then assist in the design of MMCs with optimum strength and toughness, and better resistance to impact-induced bending failure.

Section 5

PERSONNEL, ACTIVITIES, PUBLICATIONS, AND PRESENTATIONS

PERSONNEL

The following people contributed to this effort:

Richard W. Klopp, Ph.D.

Donald A. Shockey, Ph.D.

James E. Crocker

Jacques H. Giovanola, Ph.D.

John Moskito (MS candidate at San Jose State University)

ACTIVITIES

The work performed in this program and in previous AFOSR programs continues to attract the attention of the technical and scientific community. We are in frequent contact with Dr. Ted Nicholas and others at Wright Laboratory. We also have extensive interaction with Mr. Steven Kirkpatrick and Dr. Charles Schmidt, who are working at SRI on a related AFOSR research project on MMCs. Dr. Klopp has been invited to make a presentation at the Third International Conference on Composites Engineering (ICCE/3), July 21-27, 1996, in New Orleans.

PUBLICATIONS

- R. W. Klopp and J. E. Crocker, "Dynamic Fracture Behavior of SCS-6/Ti-15-3 Metal-Matrix Composite" *Int. J. Fracture* **61**:R77-R83 (1993).
- R. W. Klopp and J. E. Crocker, "A Dynamic Fiber Push-out Test Applied to Metal-Matrix Composites," *J. de Physique IV*, Colloque C8, Supplément au Journal de Physique III, V. 4, 47-51 (1994).
- J. H. Giovanola, R. W. Klopp and P. Touzé, "Microdamage Observations in Dynamically Fractured Ti-10V-2Fe-3Al Microstructures and Preliminary Modeling Attempts," accepted as a poster at the IUTAM Symposium on Micromechanics of Plasticity and Damage of Multiphase Materials, Sèvres, France, August 29-September 1, 1995, to appear in the Proceedings.

J. H. Giovanola, T. Kobayashi, R. W. Klopp, and S. W. Kirkpatrick, "Continuum and Microstructural Observations in Dynamic Fracture of Ti-2Fe-3Al Microstructures," to be submitted to *Dymat Journal*.

PRESENTATIONS

J. H. Giovanola, R. W. Klopp, and P. Touzé, "Microdamage Observations in Dynamically Fractured Ti-10V-2Fe-3Al Microstructures and Preliminary Modeling Attempts," presented at the IUTAM Symposium on Micromechanics of Plasticity and Damage of Multiphase Materials, Sèvres, France, August 29-September 1, 1995.

R. W. Klopp and J. E. Crocker, "A Dynamic Fiber Push-out Test Applied to Metal-Matrix Composites," presented at *Euro Dymat 94, International Conference on Mechanical and Physical Behavior of Materials Under Dynamic Loading*, Oxford, UK, September 26-30, 1994.

REFERENCES

1. J. A. McElman, "Continuous Silicon Carbide Fiber MMCs," *Engineered Materials Handbook: v. 1. Composites* (ASM International, Metals Park, OH, 1987), pp. 858-866.
2. B. S. Majundar, G. M. Newax, and J. R. Ellis, *Met. Trans.* **24A**, 1597-1610 (1993).
3. T. P. Gabb, J. Gayda, B. A. Lerch, and G. R. Halford, *Scripta Met.* **25**, 2879-2884 (1991).
4. D. B. Marshall, B. N. Cox, and A. G. Evans, *Acta Met.* **33**, 2013-2021 (1985).
5. Y. C. Gao, Y. W. Mai, and B. Cotterell, *J. Appl. Math. Phys. (ZAMP)* **39**, 550-572 (1988).
6. J. W. Hutchinson and H. M. Jensen, *Mechanics of Materials* **9**, 139-163 (1990).
7. G. Gao and Y. Song, *J. Mech Phys. Solids* **41**, 1425-1444 (1993).
8. D. B. Marshall and W. C. Oliver, *J. Am. Ceram. Soc.* **70**, 542-548 (1987).
9. P. D. Warren, T. J. Mackin, and A. G. Evans, *Acta Met.* **40**, 1243-1249 (1992).
10. C. Liang and J. W. Hutchinson, *Mechanics of Materials* **14**, 207-221 (1993).
11. G. Meda, S. F. Hoysan, and P. S. Steif, *J. Appl. Mech.* **60**, 986-991 (1993).
12. C.K.B. Lee and R. C. Crawford, *Meas. Sci. Technol.* **4**, 931-937 (1993).
13. B. A. Lerch, Private Communication, NASA Lewis Research Center, Cleveland, OH (1994).
14. A. Dollar and P. S. Steif, *J. Am. Ceram. Soc.* **76**(4), 897-903 (1993).
15. G. C. Sih, P. C. Paris, and G. R. Irwin, *International Journal of Fracture Mechanics* **1**, 189-203 (1965).
16. J. H. Giovanola, *ASM Metals Handbook, 9th Edition, Volume 8, Mechanical Testing* (ASM International, Metals Park, OH, 1985), pp. 271-275.
17. J. H. Giovanola, *Fracture Mechanics: Seventeenth Volume, ASTM STP 905* (American Society for Testing and Materials, Philadelphia, 1986), pp. 307-328.
18. J. H. Giovanola, R. W. Klopp, D. A. Shockey, and A. T. Werner, *Proceedings of the 7th International Conference on Fracture (ICF7, Houston, 1989)*, pp. 643-650.
19. T. Nicholas, Private Communication, Air Force Wright Laboratory (1995).

20. B. A. Lerch and J. F. Saltsman, "Tensile Deformation Damage in SiC Reinforced Ti-15V-3Cr-3Al-3Sn," NASA Technical Memorandum 103620, April 1991.
21. R. G. Whirley and B. E. Engelmann, DYNA2D A Nonlinear, Explicit, Two-Dimensional Finite Element Code for Solid Mechanics User Manual, UCRL-MA-110630 (Lawrence Livermore National Laboratory, Livermore, CA, 1992).
22. B. Antoun, Private Communication, Rensselaer Polytechnic Institute, Troy, NY (1995).
23. J. O. Hallquist, MAZE—An Input Generator for DYNA2D and NIKE2D, Report No. UCID-19029, Rev. 2, University of California (Lawrence Livermore National Laboratory, 1983).
24. T. Kobayashi and D. A. Shockey, "Microfailure Mechanisms in an Elevated Temperature Tensile Specimen," SRI International Technical Report for the University of Dayton Research Institute, Dayton, Ohio, January 1994.

**APPENDIX: MAZE [23] INPUT FILE FOR DYNA2D [21] MODEL OF MMC
NOTCHED BEND FAILURE**

APPENDIX

MAZE [23] INPUT FILE FOR DYNA2D [21] MODEL OF MMC NOTCHED BEND FAILURE

```
1
NOFR      C NO FRAME IN PLOTS (FASTER)
PPOFF     C DON'T PLOT LINES OR INDIVIDUAL PARTS
LPOFF
C
C SET TOLERANCE
C
MAZTL 1.00E-8
C
C DIMENSIONS IN METERS KILOGRAMS SECONDS
C
LD 1 LP 2 0.0000E+00 0.0000E+00 18.8600E-03 0.0000E+00
LD 2 LSTL 1 0.0000E+00 -3.8100E-03
LD 3 LSTL 1 0.0000E+00 5.7000E-03
LD 4 LP 2 0.0000E+00 -3.8100E-03 0.0000E+00 5.7000E-03
LD 5 LSTL 4 0.1270E-03 0.0000E+00
LD 6 LSTL 4 0.198125E-03 0.0000E+00
LD 7 LSTL 4 0.39625E-03 0.0000E+00
LD 8 LSTL 4 0.7925E-03 0.0000E+00
LD 9 LSTL 4 1.18875E-03 0.0000E+00
LD 10 LSTL 4 1.5850E-03 0.0000E+00
LD 11 LSTL 4 0.198125E-03 0.0000E+00
LD 12 LSTL 4 18.8600E-03 0.0000E+00
LD 13 LSTL 4 9.5100E-03 0.0000E+00
LD 14 LP 1 0.0000E+00 0.0000E+00
LAP 0.1270E-03 -0.1270E-03 0.0000E+00 -0.1270E-03
LD 15 LP 2 0.0000E+00 -0.1270E-03 0.198125E-03 0.071125E-03
C DO LAYERS DOWNWARD
LD 16 LSTL 1 0.0000E+00 -60.9583E-06
LD 17 LSTL 16 0.0000E+00 -66.0417E-06
LD 18 LSTL 17 0.0000E+00 -132.0833E-06
LD 19 LSTL 18 0.0000E+00 -66.0417E-06
LD 20 LSTL 19 0.0000E+00 -132.0833E-06
LD 21 LSTL 20 0.0000E+00 -66.0417E-06
LD 22 LSTL 21 0.0000E+00 -132.0833E-06
LD 23 LSTL 22 0.0000E+00 -66.0417E-06
LD 24 LSTL 23 0.0000E+00 -132.0833E-06
LD 25 LSTL 24 0.0000E+00 -66.0417E-06
LD 26 LSTL 25 0.0000E+00 -132.0833E-06
LD 27 LSTL 26 0.0000E+00 -66.0417E-06
```

LD 28	LSTL 27	0.0000E+00	-132.0833E-06
LD 29	LSTL 28	0.0000E+00	-66.0417E-06
LD 30	LSTL 29	0.0000E+00	-132.0833E-06
LD 31	LSTL 30	0.0000E+00	-66.0417E-06
LD 32	LSTL 31	0.0000E+00	-132.0833E-06
LD 33	LSTL 32	0.0000E+00	-66.0417E-06
LD 34	LSTL 33	0.0000E+00	-132.0833E-06
LD 35	LSTL 34	0.0000E+00	-66.0417E-06
LD 36	LSTL 35	0.0000E+00	-132.0833E-06
LD 37	LSTL 36	0.0000E+00	-66.0417E-06
LD 38	LSTL 37	0.0000E+00	-132.0833E-06
LD 39	LSTL 38	0.0000E+00	-66.0417E-06
LD 40	LSTL 39	0.0000E+00	-132.0833E-06
LD 41	LSTL 40	0.0000E+00	-66.0417E-06
LD 42	LSTL 41	0.0000E+00	-132.0833E-06
LD 43	LSTL 42	0.0000E+00	-66.0417E-06
LD 44	LSTL 43	0.0000E+00	-132.0833E-06
LD 45	LSTL 44	0.0000E+00	-66.0417E-06
LD 46	LSTL 45	0.0000E+00	-132.0833E-06
LD 47	LSTL 46	0.0000E+00	-66.0417E-06
LD 48	LSTL 47	0.0000E+00	-132.0833E-06
LD 49	LSTL 48	0.0000E+00	-66.0417E-06
LD 50	LSTL 49	0.0000E+00	-132.0833E-06
LD 51	LSTL 50	0.0000E+00	-66.0417E-06
LD 52	LSTL 51	0.0000E+00	-132.0833E-06
LD 53	LSTL 52	0.0000E+00	-66.0417E-06
LD 54	LSTL 53	0.0000E+00	-116.75E-06
C DO LAYERS UPWARD			
LD 55	LSTL 1	0.0000E+00	71.125E-06
LD 56	LSTL 55	0.0000E+00	66.0417E-06
LD 57	LSTL 56	0.0000E+00	132.0833E-06
LD 58	LSTL 57	0.0000E+00	66.0417E-06
LD 59	LSTL 58	0.0000E+00	132.0833E-06
LD 60	LSTL 59	0.0000E+00	66.0417E-06
LD 61	LSTL 60	0.0000E+00	132.0833E-06
LD 62	LSTL 61	0.0000E+00	66.0417E-06
LD 63	LSTL 62	0.0000E+00	132.0833E-06
LD 64	LSTL 63	0.0000E+00	66.0417E-06
LD 65	LSTL 64	0.0000E+00	132.0833E-06
LD 66	LSTL 65	0.0000E+00	66.0417E-06
LD 67	LSTL 66	0.0000E+00	132.0833E-06
LD 68	LSTL 67	0.0000E+00	66.0417E-06
LD 69	LSTL 68	0.0000E+00	132.0833E-06
LD 70	LSTL 69	0.0000E+00	66.0417E-06
LD 71	LSTL 70	0.0000E+00	132.0833E-06
LD 72	LSTL 71	0.0000E+00	66.0417E-06
LD 73	LSTL 72	0.0000E+00	132.0833E-06
LD 74	LSTL 73	0.0000E+00	66.0417E-06
LD 75	LSTL 74	0.0000E+00	132.0833E-06
LD 76	LSTL 75	0.0000E+00	66.0417E-06
LD 77	LSTL 76	0.0000E+00	132.0833E-06

LD 78	LSTL 77	0.0000E+00	66.0417E-06
LD 79	LSTL 78	0.0000E+00	132.0833E-06
LD 80	LSTL 79	0.0000E+00	66.0417E-06
LD 81	LSTL 80	0.0000E+00	132.0833E-06
LD 82	LSTL 81	0.0000E+00	66.0417E-06
LD 83	LSTL 82	0.0000E+00	132.0833E-06
LD 84	LSTL 83	0.0000E+00	66.0417E-06
LD 85	LSTL 84	0.0000E+00	132.0833E-06
LD 86	LSTL 85	0.0000E+00	66.0417E-06
LD 87	LSTL 86	0.0000E+00	132.0833E-06
LD 88	LSTL 87	0.0000E+00	66.0417E-06
LD 89	LSTL 88	0.0000E+00	132.0833E-06
LD 90	LSTL 89	0.0000E+00	66.0417E-06
LD 91	LSTL 90	0.0000E+00	132.0833E-06
LD 92	LSTL 91	0.0000E+00	66.0417E-06
LD 93	LSTL 92	0.0000E+00	132.0833E-06
LD 94	LSTL 93	0.0000E+00	66.0417E-06
LD 95	LSTL 94	0.0000E+00	132.0833E-06
LD 96	LSTL 95	0.0000E+00	66.0417E-06
LD 97	LSTL 96	0.0000E+00	132.0833E-06
LD 98	LSTL 97	0.0000E+00	66.0417E-06
LD 99	LSTL 98	0.0000E+00	132.0833E-06
LD 100	LSTL 99	0.0000E+00	66.0417E-06
LD 101	LSTL 100	0.0000E+00	132.0833E-06
LD 102	LSTL 101	0.0000E+00	66.0417E-06
LD 103	LSTL 102	0.0000E+00	132.0833E-06
LD 104	LSTL 103	0.0000E+00	66.0417E-06
LD 105	LSTL 104	0.0000E+00	132.0833E-06
LD 106	LSTL 105	0.0000E+00	66.0417E-06
LD 107	LSTL 106	0.0000E+00	132.0833E-06
LD 108	LSTL 107	0.0000E+00	66.0417E-06
LD 109	LSTL 108	0.0000E+00	132.0833E-06
LD 110	LSTL 109	0.0000E+00	66.0417E-06
LD 111	LSTL 110	0.0000E+00	132.0833E-06
LD 112	LSTL 13	1188.75E-06	0.000E+00
C			
C DEFINE PARTS			
C			
C BEGIN PART NUMBERING WITH NUMERAL 1 FOR ELEMENTS			
C			
C BPN 1			
C			
C MAZTL 1.00E-8			
C			
C PARTS DOWNWARD			
PART	5	18 7 17 2 8 16	Y C 1
PART	5	19 7 18 1 4 16	Y C 2
PART	5	20 7 19 2 8 16	Y C 3
PART	5	21 7 20 1 4 16	Y C 4
PART	5	22 7 21 2 8 16	Y C 5
PART	5	23 7 22 1 4 16	Y C 6

PART	5	24	7	23	2	8	16	Y	C	7
PART	5	25	7	24	1	4	16	Y	C	8
PART	5	26	7	25	2	8	16	Y	C	9
PART	5	27	7	26	1	4	16	Y	C	10
PART	5	28	7	27	2	8	16	Y	C	11
PART	5	29	7	28	1	4	16	Y	C	12
PART	5	30	7	29	2	8	16	Y	C	13
PART	5	31	7	30	1	4	16	Y	C	14
PART	5	32	7	31	2	8	16	Y	C	15
PART	5	33	7	32	1	4	16	Y	C	16
PART	5	34	7	33	2	8	16	Y	C	17
PART	5	35	7	34	1	4	16	Y	C	18
C PARTS UPWARD										
PART	4	55	7	56	1	4	24	Y	C	19
PART	4	56	7	57	2	8	24	Y	C	20
PART	4	57	7	58	1	4	24	Y	C	21
PART	4	58	7	59	2	8	24	Y	C	22
PART	4	59	7	60	1	4	24	Y	C	23
PART	4	60	7	61	2	8	24	Y	C	24
PART	4	61	7	62	1	4	24	Y	C	25
PART	4	62	7	63	2	8	24	Y	C	26
PART	4	63	7	64	1	4	24	Y	C	27
PART	4	64	7	65	2	8	24	Y	C	28
PART	4	65	7	66	1	4	24	Y	C	29
PART	4	66	7	67	2	8	24	Y	C	30
PART	4	67	7	68	1	4	24	Y	C	31
PART	4	68	7	69	2	8	24	Y	C	32
PART	4	69	7	70	1	4	24	Y	C	33
PART	4	70	7	71	2	8	24	Y	C	34
PART	4	71	7	72	1	4	24	Y	C	35
PART	4	72	7	73	2	8	24	Y	C	36
PART	4	73	7	74	1	4	24	Y	C	37
PART	4	74	7	75	2	8	24	Y	C	38
PART	4	75	7	76	1	4	24	Y	C	39
PART	4	76	7	77	2	8	24	Y	C	40
PART	4	77	7	78	1	4	24	Y	C	41
PART	4	78	7	79	2	8	24	Y	C	42
PART	4	79	7	80	1	4	24	Y	C	43
PART	4	80	7	81	2	8	24	Y	C	44
PART	4	81	7	82	1	4	24	Y	C	45
PART	4	82	7	83	2	8	24	Y	C	46
PART	4	83	7	84	1	4	24	Y	C	47
PART	4	84	7	85	2	8	24	Y	C	48
PART	4	85	7	86	1	4	24	Y	C	49
PART	4	86	7	87	2	8	24	Y	C	50
PART	4	87	7	88	1	4	24	Y	C	51
PART	4	88	7	89	2	8	24	Y	C	52
PART	4	89	7	90	1	4	24	Y	C	53
PART	4	90	7	91	2	8	24	Y	C	54
PART	4	91	7	92	1	4	24	Y	C	55
PART	4	92	7	93	2	8	24	Y	C	56

PART 4 93 7 94 1 4 24 Y	C 57
C NOTCH ROOT PARTS	
PART 14 17 7 16 1 4 16 Y	C 58
PART 6 16 7 55 2 8 12 Y	C 59
PART 6 15 14 16 2 8 5 Y	C 60
PART 55 4 14 15 2 12 5 Y	C 61
MG 59 60	
MG 59 61	
C PARTS TO THE RIGHT & DOWNWARD	
T12	
PART 8 17 7 18 2 4 12 Y	C 62
T12	
PART 8 18 7 19 1 2 12 Y	C 63
T12	
PART 8 19 7 20 2 4 12 Y	C 64
T12	
PART 8 20 7 21 1 2 12 Y	C 65
T12	
PART 8 21 7 22 2 4 12 Y	C 66
T12	
PART 8 22 7 23 1 2 12 Y	C 67
T12	
PART 8 23 7 24 2 4 12 Y	C 68
T12	
PART 8 24 7 25 1 2 12 Y	C 69
T12	
PART 8 25 7 26 2 4 12 Y	C 70
T12	
PART 8 26 7 27 1 2 12 Y	C 71
T12	
PART 8 27 7 28 2 4 12 Y	C 72
T12	
PART 8 28 7 29 1 2 12 Y	C 73
T12	
PART 8 29 7 30 2 4 12 Y	C 74
T12	
PART 8 30 7 31 1 2 12 Y	C 75
T12	
PART 8 31 7 32 2 4 12 Y	C 76
T12	
PART 8 32 7 33 1 2 12 Y	C 77
T12	
PART 8 33 7 34 2 4 12 Y	C 78
T12	
PART 8 34 7 35 1 2 12 Y	C 79
C PARTS TO THE LEFT & UPWARD	
T12	
PART 8 56 7 55 1 2 12 Y	C 80
T12	
PART 8 57 7 56 2 4 12 Y	C 81
T12	

PART	8	58	7	57	1	2	12	Y	C	82
TL2										
PART	8	59	7	58	2	4	12	Y	C	83
TL2										
PART	8	60	7	59	1	2	12	Y	C	84
TL2										
PART	8	61	7	60	2	4	12	Y	C	85
TL2										
PART	8	62	7	61	1	2	12	Y	C	86
TL2										
PART	8	63	7	62	2	4	12	Y	C	87
TL2										
PART	8	64	7	63	1	2	12	Y	C	88
TL2										
PART	8	65	7	64	2	4	12	Y	C	89
TL2										
PART	8	66	7	65	1	2	12	Y	C	90
TL2										
PART	8	67	7	66	2	4	12	Y	C	91
TL2										
PART	8	68	7	67	1	2	12	Y	C	92
TL2										
PART	8	69	7	68	2	4	12	Y	C	93
TL2										
PART	8	70	7	69	1	2	12	Y	C	94
TL2										
PART	8	71	7	70	2	4	12	Y	C	95
TL2										
PART	8	72	7	71	1	2	12	Y	C	96
TL2										
PART	8	73	7	72	2	4	12	Y	C	97
TL2										
PART	8	74	7	73	1	2	12	Y	C	98
TL2										
PART	8	75	7	74	2	4	12	Y	C	99
TL2										
PART	8	76	7	75	1	2	12	Y	C	100
TL2										
PART	8	77	7	76	2	4	12	Y	C	101
TL2										
PART	8	78	7	77	1	2	12	Y	C	102
TL2										
PART	8	79	7	78	2	4	12	Y	C	103
TL2										
PART	8	80	7	79	1	2	12	Y	C	104
TL2										
PART	8	81	7	80	2	4	12	Y	C	105
TL2										
PART	8	82	7	81	1	2	12	Y	C	106
TL2										
PART	8	83	7	82	2	4	12	Y	C	107

PART	9	27	8	28	2	2	6	Y	C	131
T12										
PART	9	28	8	29	1	1	6	Y	C	132
T12										
PART	9	29	8	30	2	2	6	Y	C	133
T12										
PART	9	30	8	31	1	1	6	Y	C	134
T12										
PART	9	31	8	32	2	2	6	Y	C	135
T12										
PART	9	32	8	33	1	1	6	Y	C	136
T12										
PART	9	33	8	34	2	2	6	Y	C	137
T12										
PART	9	34	8	35	1	1	6	Y	C	138
C										
C	PARTS TO THE LEFT & UPWARD									
T12										
PART	9	56	8	55	1	1	6	Y	C	139
T12										
PART	9	57	8	56	2	2	6	Y	C	140
T12										
PART	9	58	8	57	1	1	6	Y	C	141
T12										
PART	9	59	8	58	2	2	6	Y	C	142
T12										
PART	9	60	8	59	1	1	6	Y	C	143
T12										
PART	9	61	8	60	2	2	6	Y	C	144
T12										
PART	9	62	8	61	1	1	6	Y	C	145
T12										
PART	9	63	8	62	2	2	6	Y	C	146
T12										
PART	9	64	8	63	1	1	6	Y	C	147
T12										
PART	9	65	8	64	2	2	6	Y	C	148
T12										
PART	9	66	8	65	1	1	6	Y	C	149
T12										
PART	9	67	8	66	2	2	6	Y	C	150
T12										
PART	9	68	8	67	1	1	6	Y	C	151
T12										
PART	9	69	8	68	2	2	6	Y	C	152
T12										
PART	9	70	8	69	1	1	6	Y	C	153
T12										
PART	9	71	8	70	2	2	6	Y	C	154
T12										
PART	9	72	8	71	1	1	6	Y	C	155

[illegible]

C MERGE PARTS

C

C PARTS DOWNWARD

MG	1	62	MG	1	121
MG	2	63	MG	2	122
MG	3	64	MG	3	123
MG	4	65	MG	4	124
MG	5	66	MG	5	125
MG	6	67	MG	6	126
MG	7	68	MG	7	127
MG	8	69	MG	8	128
MG	9	70	MG	9	129
MG	10	71	MG	10	130
MG	11	72	MG	11	131
MG	12	73	MG	12	132
MG	13	74	MG	13	133
MG	14	75	MG	14	134
MG	15	76	MG	15	135
MG	16	77	MG	16	136
MG	17	78	MG	17	137
MG	18	79	MG	18	138

C PARTS UPWARD

MG	19	80	MG	19	139
MG	20	81	MG	20	140
MG	21	82	MG	21	141
MG	22	83	MG	22	142
MG	23	84	MG	23	143
MG	24	85	MG	24	144
MG	25	86	MG	25	145
MG	26	87	MG	26	146
MG	27	88	MG	27	147
MG	28	89	MG	28	148
MG	29	90	MG	29	149
MG	30	91	MG	30	150
MG	31	92	MG	31	151
MG	32	93	MG	32	152
MG	33	94	MG	33	153
MG	34	95	MG	34	154
MG	35	96	MG	35	155
MG	36	97	MG	36	156
MG	37	98	MG	37	157
MG	38	99	MG	38	158
MG	39	100	MG	39	159
MG	40	101	MG	40	160
MG	41	102	MG	41	161
MG	42	103	MG	42	162
MG	43	104	MG	43	163
MG	44	105	MG	44	164
MG	45	106	MG	45	165
MG	46	107	MG	46	166
MG	47	108	MG	47	167

MG	48	109	MG	48	168				
MG	49	110	MG	49	169				
MG	50	111	MG	50	170				
MG	51	112	MG	51	171				
MG	52	113	MG	52	172				
MG	53	114	MG	53	173				
MG	54	115	MG	54	174				
MG	55	116	MG	55	175				
MG	56	117	MG	56	176				
MG	57	118	MG	57	177				
C NOTCH ROOT PARTS									
MG	58	119	MG	58	178				
MG	59	120	MG	59	179				
C									
PART	4	94	7	95	2	8	24	Y	C 180
T12									
PART	8	95	7	94	2	4	12	Y	C 181
T12									
PART	9	95	8	94	2	2	6	Y	C 182
MG	180	181	MG	180	182				
C									
C HOMOGENIZED PARTS									
C									
T13									
PART	10	95	9	35	3	30	2	Y	C 183
C									
T13									
PART	13	95	10	35	3	10	13	Y	C 184
T12									
PART	12	95	13	35	3	5	8	Y	C 185
MG	183	184	MG	183	185				
C									
C UPPER HOMOGENIZED PARTS									
C									
T12									
PART	97	4	95	7	3	12	6	Y	C 186
PART	97	7	95	8	3	12	6	Y	C 187
T13									
PART	9	97	8	95	3	2	6	Y	C 188
T12									
PART	101	4	97	8	3	12	4	Y	C 189
PART	9	101	8	97	3	4	6	Y	C 190
T12									
PART	10	101	9	95	3	3	2	Y	C 191
T13									
PART	107	4	103	9	3	6	2	Y	C 192
T12									
PART	10	103	9	101	3	1	2	Y	C 193
RFLIP	193	3	Y						C 194
CLONE	194	3	0	9.454125E-03	0	Y			C 195
DP	193								

FV
 MAZTL 1.000E-07
 MG 183 205
 MAZTL 3.00E-05
 MG 183 208
 MG 183 209
 MG 183 213
 MG 183 212
 MAZTL 1.000E-08
 MG 186 189
 MG 186 199
 MG 186 192
 MG 186 201
 MG 183 186
 C
 C ASSEMBLE PARTS
 C
 ASSM
 C
 MAZTL 1.00E-08
 C
 C PARTS DOWNWARD
 GM 1 183
 GM 2 183
 GM 3 183
 GM 4 183
 GM 5 183
 GM 6 183
 GM 7 183
 GM 8 183
 GM 9 183
 GM 10 183
 GM 11 183
 GM 12 183
 GM 13 183
 GM 14 183
 GM 15 183
 GM 16 183
 GM 17 183
 GM 18 183
 C PARTS UPWARD
 GM 19 183
 GM 20 183
 GM 21 183
 GM 22 183
 GM 23 183
 GM 24 183
 GM 25 183
 GM 26 183
 GM 27 183
 GM 28 183

```

GM 29 183
GM 30 183
GM 31 183
GM 32 183
GM 33 183
GM 34 183
GM 35 183
GM 36 183
GM 37 183
GM 38 183
GM 39 183
GM 40 183
GM 41 183
GM 42 183
GM 43 183
GM 44 183
GM 45 183
GM 46 183
GM 47 183
GM 48 183
GM 49 183
GM 50 183
GM 51 183
GM 52 183
GM 53 183
GM 54 183
GM 55 183
GM 56 183
GM 57 183
GM 180 183
C NOTCH ROOT PARTS
GM 58 183
GM 59 183
C
C REDUCE NO OF SLIDELINES BY MERGING SOME CRACK WAKE PARTS AND
C MAKING THEM INTO MATERIAL 3
C
C
C FORCE RECALCITRANT NODES TOGETHER
MGN 13991 14130
C SMOOTH MESH
GS
C DISPLAY MESH
C G
C
C CONSTRAIN LIGAMENT NODES
RCON 0.00E+00
C
C DO SLIDELINES
C
SLN 1 4 2.00E-01 SLNP 1.00E+00 SLBP 180 57

```


SLN	2	4	2.00E-01	SLNP	1.00E+00	SLBP	57	56
SLN	3	4	2.00E-01	SLNP	1.00E+00	SLBP	56	55
SLN	4	4	2.00E-01	SLNP	1.00E+00	SLBP	55	54
SLN	5	4	2.00E-01	SLNP	1.00E+00	SLBP	54	53
SLN	6	4	2.00E-01	SLNP	1.00E+00	SLBP	53	52
SLN	7	4	2.00E-01	SLNP	1.00E+00	SLBP	52	51
SLN	8	4	2.00E-01	SLNP	1.00E+00	SLBP	51	50
SLN	9	4	2.00E-01	SLNP	1.00E+00	SLBP	50	49
SLN	10	4	2.00E-01	SLNP	1.00E+00	SLBP	49	48
SLN	11	4	2.00E-01	SLNP	1.00E+00	SLBP	48	47
SLN	12	4	2.00E-01	SLNP	1.00E+00	SLBP	47	46
SLN	13	4	2.00E-01	SLNP	1.00E+00	SLBP	46	45
SLN	14	4	2.00E-01	SLNP	1.00E+00	SLBP	45	44
SLN	15	4	2.00E-01	SLNP	1.00E+00	SLBP	44	43
SLN	16	4	2.00E-01	SLNP	1.00E+00	SLBP	43	42
SLN	17	4	2.00E-01	SLNP	1.00E+00	SLBP	42	41
SLN	18	4	2.00E-01	SLNP	1.00E+00	SLBP	41	40
SLN	19	4	2.00E-01	SLNP	1.00E+00	SLBP	40	39
SLN	20	4	2.00E-01	SLNP	1.00E+00	SLBP	39	38
SLN	21	4	2.00E-01	SLNP	1.00E+00	SLBP	38	37
SLN	22	4	2.00E-01	SLNP	1.00E+00	SLBP	37	36
SLN	23	4	2.00E-01	SLNP	1.00E+00	SLBP	36	35
SLN	24	4	2.00E-01	SLNP	1.00E+00	SLBP	35	34
SLN	25	4	2.00E-01	SLNP	1.00E+00	SLBP	34	33
SLN	26	4	2.00E-01	SLNP	1.00E+00	SLBP	33	32
SLN	27	4	2.00E-01	SLNP	1.00E+00	SLBP	32	31
SLN	28	4	2.00E-01	SLNP	1.00E+00	SLBP	31	30
SLN	29	4	2.00E-01	SLNP	1.00E+00	SLBP	30	29
SLN	30	4	2.00E-01	SLNP	1.00E+00	SLBP	29	28
SLN	31	4	2.00E-01	SLNP	1.00E+00	SLBP	28	27
SLN	32	4	2.00E-01	SLNP	1.00E+00	SLBP	27	26
SLN	33	4	2.00E-01	SLNP	1.00E+00	SLBP	26	25
SLN	34	4	2.00E-01	SLNP	1.00E+00	SLBP	25	24
SLN	35	4	2.00E-01	SLNP	1.00E+00	SLBP	24	23
SLN	36	4	2.00E-01	SLNP	1.00E+00	SLBP	23	22
SLN	37	4	2.00E-01	SLNP	1.00E+00	SLBP	22	21
SLN	38	4	2.00E-01	SLNP	1.00E+00	SLBP	21	20
SLN	39	4	2.00E-01	SLNP	1.00E+00	SLBP	20	19
SLN	40	4	2.00E-01	SLNP	1.00E+00	SLBP	19	59
SLN	41	4	2.00E-01	SLNP	1.00E+00	SLBP	59	58
SLN	42	4	2.00E-01	SLNP	1.00E+00	SLBP	58	1
SLN	43	4	2.00E-01	SLNP	1.00E+00	SLBP	1	2
SLN	44	4	2.00E-01	SLNP	1.00E+00	SLBP	2	3
SLN	45	4	2.00E-01	SLNP	1.00E+00	SLBP	3	4
SLN	46	4	2.00E-01	SLNP	1.00E+00	SLBP	4	5
SLN	47	4	2.00E-01	SLNP	1.00E+00	SLBP	5	6
SLN	48	4	2.00E-01	SLNP	1.00E+00	SLBP	6	7
SLN	49	4	2.00E-01	SLNP	1.00E+00	SLBP	7	8
SLN	50	4	2.00E-01	SLNP	1.00E+00	SLBP	8	9
SLN	51	4	2.00E-01	SLNP	1.00E+00	SLBP	9	10
SLN	52	4	2.00E-01	SLNP	1.00E+00	SLBP	10	11

```

SLN  53  4  2.00E-01  SLNP  1.00E+00  SLBP  11  12
SLN  54  4  2.00E-01  SLNP  1.00E+00  SLBP  12  13
SLN  55  4  2.00E-01  SLNP  1.00E+00  SLBP  13  14
SLN  56  4  2.00E-01  SLNP  1.00E+00  SLBP  14  15
SLN  57  4  2.00E-01  SLNP  1.00E+00  SLBP  15  16
SLN  58  4  2.00E-01  SLNP  1.00E+00  SLBP  16  17
SLN  59  4  2.00E-01  SLNP  1.00E+00  SLBP  17  18
C
C  DEFINE LOAD CURVE (SECONDS  NEWTONS  SECONDS  NEWTONS)
C
LCD  1  4  0.0  0.0  0.5E-06  -1.5E+01  1.00E-06  -3.00E+01  30.00E-06
      -3.00E+01
C
C
P  183  B
VBC  14778  14781  1  1.000  1.000  2
C
C
PLANE                                C PLANE STRAIN (DEFAULT IS AXISYMMETRIC)
C
TITLE
3-POINT NOTCHED BEND BAR WITH FIBER TENSILE FAILURE
C
C  ANALYSIS PARAMETERS
C
PLTI  1.00E-06                      C PLOT INFO EVERY STEP
PRTI  1.00E-06                      C PRINT INFO EVERY STEP
C
TERM  10.00E-06
WBCD DYNA2D                          C WRITE INPUT FILE FOR DYNA2D
C
C  HOURGLASS VISCOSITY PARAMETERS
C
DHQT  3
DHGQ  0.390
C
C  DEFINE MATERIALS
C
MAT  1  10  HEADING
SIC
RO  3.100E3  C  KG/M3                C  DENSITY
G  160.0E+09  C  N/M2                C  YOUNG'S MODULUS
C  PR  0.25                      C  POISSON'S RATIO
SIGY  10.0E+09                      C  YIELD STRESS
EH  400.0E+09                      C  PLASTIC MODULUS
PC  -3.2E+09                      C  PC=PCUT=MAX PRINC NORMAL STRESS CUTOFF
A1  0.0                      C  LINEAR PRESSURE HARDENING COEFF
A2  0.0                      C  QUADRATIC PRESSURE HARDENING COEFF
SPALL  2.0                      C  IF MAX PRINC STRESS EXCEEDS
C                      C  -PCUT, STRESS DEVIATOR IS ZEROED
C                      C  AND HYDROSTATIC TENSION IS PRECLUDED.

```

ENDMAT

C

EOS 1 1

HEAD SIC EOS

C1 267.0E+09

ENDEOS

C

MAT 2 3 HEADING

TITANIUM

RO 4.650E3 C KG/M3

E 82.0E+09 C N/M2

PR 0.32

SIGY 0.876E+09

ETAN 0.000E+00

BETA 1

ENDMAT

C

MAT 3 3 HEADING

TITANIUM SIC MIXTURE

RO 3.617E3 C KG/M3

E 203.0E+09 C N/M2

PR 0.27

SIGY 1.455E+09

ETAN 0.000E+00

BETA 1

ENDMAT

C

END

C BULK MODULUS

C DENSITY

C YOUNG'S MODULUS

C POISSON'S RATIO

C N/M2 YIELD STRESS

C N/M2 TANGENT MODULUS

C ISOTROPIC HARDENING

C DENSITY

C YOUNG'S MODULUS

C POISSON'S RATIO

C N/M2 YIELD STRESS

C N/M2 TANGENT MODULUS

C ISOTROPIC HARDENING